Ocean surface currents derived from Sentinel-1 SAR Doppler shift measurements

Artem Moiseev

Thesis for the degree of Philosophiae Doctor (PhD)
University of Bergen, Norway
2021

UNIVERSITY OF BERGEN

Ocean surface currents derived from Sentinel-1 SAR Doppler shift measurements

Artem Moiseev

Thesis for the degree of Philosophiae Doctor (PhD)
at the University of Bergen

Date of defense: 20.05.2021

Year: 2021

Title: Ocean surface currents derived from Sentinel-1 SAR Doppler shift measurements

Name: Artem Moiseev

Print: Skipnes Kommunikasjon / University of Bergen

Scientific enviroment

The thesis was carried out at the Nansen Environmental and Remote Sensing Center (NERSC) in Bergen, Norway, where I was part of the Ocean and Sea Ice Remote Sensing (OSIRS) group. The work was supported by the Research Council of Norway uSeaSat project under contract number 251348/F50 and by the Centre for Integrated Remote Sensing and Forecasting for Arctic Operations (CIRFA) project number 970422528. During my PhD study period, I spent nine months at the CIRFA in Tromsø, Norway, where I was part of the Ocean Remote Sensing group. I was also part of the Norwegian Research School on Changing Climates in the Coupled Earth System (CHESS). The Sentinel-1 SAR products used in this study were available thanks to the ESA-ESRIN Sentinel-1 SAR Radial Velocity (RVL) Assessment Project and the Copernicus program. The SAR data processing tool was provided by the NORCE Norwegian Research Centre AS.

Acknowledgements

First and foremost, I would like to express my sincere gratitude to Johnny A. Johannessen for both largely giving me the freedom to pursue my research at my own pace while at the same time giving support and guidance whenever necessary. I also would like to thank my co-supervisor, Morten W. Hansen, for the support and help with understanding the basics of SAR. Finally, I want to thank my co-supervisor, Harald Johnsen, for hosting my research at the CIRFA and the great collaboration that made up the major part of the thesis. You all contributed with your dedication and always had time for discussions and solving all sorts of problems. Without your help, this thesis would not have been feasible within the allocated time.

I am also grateful to my colleagues in the OSIRS group, and especially to Anton Korosov for his much-needed help with understanding the geospatial nature of the data, advice on programming, and support. My sincere thanks also go to the administrative, technical, and scientific staff at the Nansen center for all their help and for providing an excellent social and scientifically stimulating environment. Among others, I would also like to thank Fabrice Collard, Bertrand Chapron, Vladimir Kudryavtsev, Kai H. Christensen, and Mostafa Bakhoday Paskyabi for their expertise and advice at different stages of the project.

Finally, I would like to thank my family, close friends, and many others for all their support.

Abstract

Reliable information about ocean surface currents is crucial for operational oceanography, regulating weather development, and climate research (e.g., UN SDG 13). Upper-ocean currents are also key for monitoring life below water, including conservation of marine biodiversity at every trophic level (e.g., UN SDG 14). Locating upper ocean currents "with the right strength at the right place and time" is moreover critically needed to support the maritime transport sector, renewable marine energy, and maritime safety operations as well as for monitoring and tracking of marine pollution. In spite of this, upper ocean currents and their variability are mostly indirectly estimated and often without quantitative knowledge of uncertainties.

In this thesis, Sentinel-1 Synthetic Aperture Radar (SAR) based Doppler frequency shift observations are examined for the retrievals of ocean surface current velocity in the radar line-of-sight direction. In the first study (Paper 1), Sentinel-1 A/B Interferometric Wide (IW) data acquired along the northern part of the Norwegian coastal zone from October-November 2017 at a spatial resolution of 1.5 km are compared with independent in-situ data, ocean model fields, and coastal High-Frequency Radar observations. Although only a limited dataset was available, the findings and results reveal that the strength of the meandering Norwegian Coastal Current derived from the SAR Doppler frequency shift observations are consistent with observations. However, limitations are encountered due to insufficient calibration and lack of ability to properly partition the geophysical signals into wave and current contributions.

A novel approach for calibration of the attitude contribution to the Sentinel-1B Wave Mode (WV) Doppler frequency shift emerged for a test period in December 2017 - January 2018. Building on this calibrated dataset, an empirical model function (CDOP3S) for prediction of the sea state-induced contribution to the Doppler shift observations is developed for the global open ocean in Paper 2. The assessment against collocated surface drifter data are promising and suggest that the Sentinel-1B WV

acquisitions can be used to study the equatorial ocean surface currents at a monthly timescale with a 20 km spatial resolution.

The calibrated dataset combined with the new Geophysical Model Function (GMF) developed in Paper 2 also allowed for the study (Paper 3) of ocean surface current retrievals from the high-resolution Sentinel-1B IW swath data acquired along the coastal zone on northern Norway. In this case, the GMF had to be trained and adjusted for fetch limited coastal sea state conditions. The results demonstrate that the Sentinel-1B SAR-derived ocean surface currents significantly improved, compared to the findings reported in Paper 1.

Although the thesis builds on a limited period of observations, constrained by the availability of experimental attitude calibration, the results are all in all promising. Reprocessing of the full Sentinel-1 A/B SAR Doppler shift dataset using the novel attitude bias correction is therefore strongly recommended for further improvement of the empirical model function. Regular use of the Sentinel-1 A/B SAR for ocean surface current monitoring would thus be feasible, leading to advances in studies of upper ocean dynamics in support to the Copernicus Marine Environment Monitoring Service (CMEMS) program and the United Nations (UN) Decade of Ocean Sciences.

List of Publications

Moiseev, A., Johnsen, H., Hansen, M. W., & Johannessen, J. A. (2020). Evaluation of radial ocean surface currents derived from Sentinel-1 IW Doppler shift using coastal radar and Lagrangian surface drifter observations. Journal of Geophysical Research: Oceans, 125, e2019JC015743. https://doi.org/10.1029/2019JC015743

Moiseev, A., Johnsen, H., Johannessen, J. A., Collard, F., & Guitton, G. (2020). On removal of sea state contribution to Sentinel-1 Doppler shift for retrieving Reliable Ocean surface current. Journal of Geophysical Research: Oceans, 125, e2020JC016288. https://doi.org/10.1029/2020JC016288

Moiseev, A., Johannessen, J.A., Johnsen, H., (2020). Towards Retrieving Reliable Ocean Surface Currents in the Coastal Zone from the Sentinel-1 Doppler Shift Observations. Journal of Geophysical Research: Oceans *(In review)*

Contents

1. Chapter 1 - Introduction

Reliable information about ocean surface currents is crucial for operational oceanography, weather development, and climate research. Ocean currents in the surface layer are composed of different contributing sources such as geostrophic current, Ekman current, wave-induced Stokes drift, inertial motion, and tidal current. Ocean surface current observations are usually available from in-situ sensors located on drifting buoys (Haza et al., 2018; Lumpkin & Johnson, 2013; Maximenko et al., 2013), shipboard, and anchored moorings. Although these observations are the most accurate, they are also challenging to collect and, hence, irregular in time and space. Several remote sensing techniques have emerged over the last decades to complement in-situ current measurements. The land-based High-Frequency Radars (HFRs) proven to be useful for real-time monitoring of the ocean surface currents in the coastal zones (Barrick et al., 1977), to support oil spill tracking (Abascal et al., 2017), and for search-and-rescue operations (Breivik et al., 2013). Despite the attractive temporal-spatial resolution, these observations typically cover a limited coastal area (order 100 km) around a fixed antenna. Satellite-based surface current observations are predominantly provided by the radar altimetry, which delivers geostrophic currents in the open ocean (Johannessen et al., 2014; Le Traon et al., 2015). However, these observations have a coarse temporal-spatial resolution (about 20 km and 25 days for the gridded products) and, in general, are not applicable for monitoring surface currents in coastal zones.

Application of spaceborne Synthetic Aperture Radars (SARs) is rapidly increasing for sea ice classification (Korosov et al., 2018; Lohse et al., 2020; Zakhvatkina et al., 2019), oil spill detection (Espeseth et al., 2020; Johansson et al., 2020), and near-surface wind speed (Dagestad et al., 2012; Nilsen et al., 2019; Stopa et al., 2017) and wave (Stopa et al., 2017) retrievals. Moreover, the phase information recorded by SAR yields the Doppler frequency shift, which, in turn, is a measure of the ocean surface motion in the radar line-of-sight (hereafter range) direction (Chapron et al., 2005; Hansen, Collard, et al., 2011; Johannessen et al., 2008; Romeiser & Thompson, 2000). The SAR-registered ocean surface motion contains contributions from the wind, wave, and ocean surface currents. Despite the challenging processing, the ocean surface

current retrievals acquired from the Envisat Advanced SAR (ASAR) instrument showed promising potential for retrieving information about strong western boundary currents (Chapron et al., 2005; Johannessen et al., 2008; Rouault et al., 2010) as well as weaker currents in the Nordic seas (Hansen, Johannessen, et al., 2011).

The Sentinel-1 is a constellation of two satellites (A/B) carrying C-Band SAR antennas, operating under the European Space Agency (ESA) Copernicus program, with scheduled performance beyond 2030 (with the launch of two more platforms in 2022-2023). Observations from various Sentinel-1 acquisition modes provide snapshots of the ocean surface in the open ocean and the coastal zone with increased temporal and spatial resolution compared to the legacy ASAR mission. However, the challenging calibration and partitioning of geophysical contributions to the signal between the surface current and the sea state diminished usage of the Sentinel-1 Doppler shift observations for the routine monitoring of ocean surface currents. Moreover, the lack of systematic validation compromises further development and application of this emerging method. Hence, addressing these issues will unlock the potential for operational application of the Sentinel-1 data for the following decade to support the Copernicus Marine Environment Monitoring Service (CMEMS) program and the United Nations (UN) Decade of Ocean Sciences.

In this theses, we use Sentinel-1 observations acquired over the open ocean and in the coastal zone to address the calibration and the geophysical signal separation challenges and, in turn, improve the accuracy of ocean surface current radial velocity retrievals. Relying on the wind and sea state information from the collocated numerical models, we develop an empirical Geophysical Model Function (GMF) for estimating the sea-sate-induced contribution to the recorded signal. Furthermore, we develop a framework for evaluation of the SAR derived ocean surface radial velocities using independent in-situ and remote sensing observations, as well as numerical ocean model simulations. Finally, we demonstrate the potential of Sentinel-1 Doppler shift acquisitions for retrieving high-resolution mesoscale surface current features in the coastal zone as well as monthly global surface current maps.

2. Chapter 2 - Scope of the thesis

2.1 Motivation and Objectives

The SAR Doppler frequency shift observations acquired over the ocean contain information about surface motion induced by the near-surface wind, wave, and currents in the radar range direction. The Sentinel-1 A/B, launched in 2014/2016, is an operational C-Band SAR mission providing continuous all-weather, day-and-night imagery to support operational marine monitoring and applications. The Doppler shift observations are available in the operational Sentinel-1 WaVe (WV) and Interferometric Wide (IW) Level 2 products in the open ocean and the coastal zones. However, these observations suffer from severe non-geophysical contributions due to the antenna electronic miss-pointing and rapid attitude variation. Consequently, accurate calibration of these non-geophysical contributions is essential for deriving reliable geophysical signal. Hitherto, unfortunately, the antenna and attitude contributions calculated from the antenna model and down-linked quaternions in the Sentinel-1 Level 2 processor do not correctly represent the non-geophysical variations in observations. A novel approach (OceanDataLab, 2019) for estimating the attitude contribution to the Doppler signal based on the gyroscope telemetry from the satellite has, therefore, emerged in 2019. However, this methodology has to be evaluated to assess the impact on the accuracy of geophysical retrievals.

When all non-geophysical contributions are estimated and removed, the residual geophysical Doppler frequency shift is related to the motion induced by short Bragg resonant waves and their modulation by longer waves and the underlying ocean surface currents (Chapron et al., 2005). Therefore, accurate estimates of the wave-induced contributions are required to retrieve the signal from ocean surface currents. However, deriving an analytical-based estimation of the sea state contribution is challenging due to the number and complexity of involved parameters associated with the directional wave spectra and the SAR acquisition geometry. The artificial Neural Networks (NN) provide an opportunity to approximate any arbitrary complex function without any prior knowledge of the relationship between independent and dependent data. Hence,

with careful sub-selection of the representative training SAR imagery, to avoid regions of strong surface currents and shallow coastal topography, this machine learning approach can be employed to estimate the wave-induced contribution for the given environmental conditions. Assuming the fully developed sea, an empirical GMF, such as CDOP (Mouche et al., 2012), can be used to predict the wind-wave-induced contribution to the Doppler shift for the given radar configuration and near-surface wind field from a collocated numerical model. However, using only the wind information at the SAR acquisition time, it does not account for the wind fetch, wind history, and contributions from the swell. Furthermore, the CDOP was trained to fit the ASAR observations, which can yield additional biases when applied to the Sentinel-1 data, taking into account the empirical nature of the model. Hence, the accuracy of the CDOP in application to the Sentinel-1 data has to be evaluated. Moreover, an empirical model that accounts for a realistic sea state should be developed to provide comprehensive estimates of the sea-state-induced contribution from the wind sea and swell and, in turn, improve the accuracy of ocean surface current retrievals.

The SAR-derived Doppler radial velocity is an emerging methodology for retrieving the surface current observations. Hence, the application of these data for monitoring of surface currents, as well as further development of the method, requires continuous validation and assessment. Evaluation of SAR retrievals is a challenge due to the involvement of numerous preprocessing steps as well as handling the geospatial properties of the data. Therefore a framework for routine collocation and comparison of the Sentinel-1 observations versus various in-situ and remote sensing observations, as well as model simulations, has to be developed.

In this thesis, we address the following objectives with the main goal to improve the accuracy of the ocean surface current retrievals from the Sentinel-1 SAR in the global open ocean and the Norwegian coastal zone:

1. Implement the methodology and evaluate non-geophysical contributions to the Doppler frequency shift observations acquired in the Interferometric Wide (IW)

and WaVe (WV) modes. Provide estimates of the signal accuracy based on observations acquired over the land.

2. Develop an empirical GMF for estimating the sea-state-induced contribution to the signal, based on calibrated Doppler shift observations collocated with the near-surface wind and ocean surface wave fields from corresponding numerical models.
3. Validate Sentinel-1 Doppler frequency shift observations using independent in-situ and remote sensing observations.
4. Demonstrate the potential of Sentinel-1 acquisitions to retrieve reliable ocean surface currents in the global open ocean and the Norwegian coastal zone.

2.2 Retrieving ocean surface current radial velocity from the Sentinel-1 Doppler frequency shift

2.2.1 Sentinel-1 Doppler shift acquisitions

In this thesis, we use Sentinel-1 Level 2 Ocean (OCN) Radial Velocity (RVL) products from the WaVe (WV) and the Interferometric Wide (IW) modes (Figure 1) respectively acquired over the global open ocean and in the Norwegian coastal zone. The independent WV vignettes with spatial coverage of 20x20 km and pixel size of 5x5 m are acquired every 100 km along the satellite track over the open ocean in a leap-frog pattern at two incidence angles $\theta_{wv1} = 23°$ and $\theta_{wv2} = 36°$. To increase the signal-to-noise ratio (SNR) and simplify the analysis the signals from all pixels within the vignette were averaged yielding a single RVL product with resolution of 20x20 km. In contrast, each IW scene consists of 3 sub swaths, with a total width of 250 km, acquired in the TOPSAR mode at incidence angles between $\theta = 29.1°$ and $\theta = 46.0°$. The spatial resolution of the Level 2 IW products used in this study is 1.5 km.

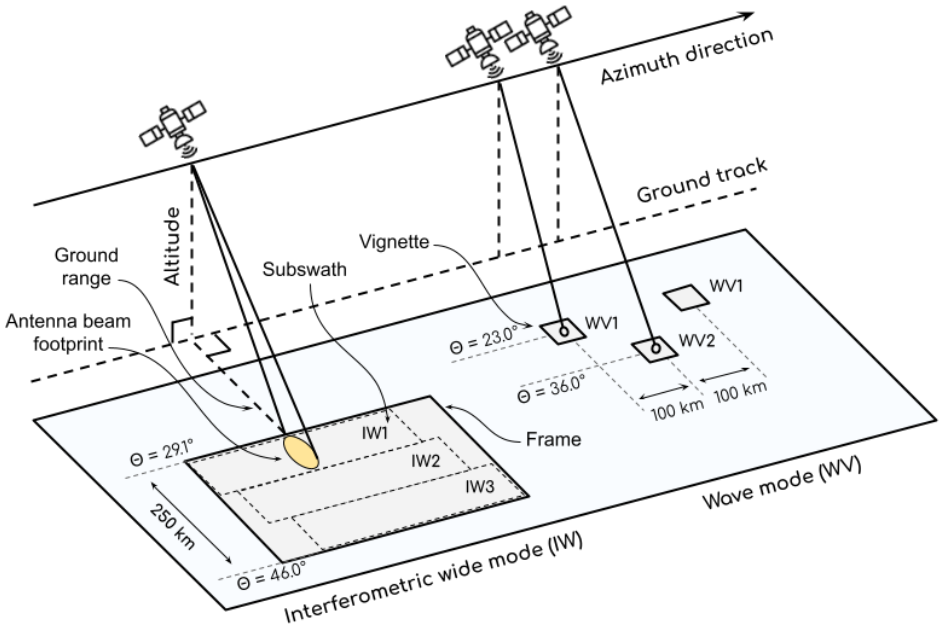

Figure 1. Acquisition modes available from the Senitnel-1 Synthetic Aperture Radar: (left) Interferometric Wide (IW) mode swaths - available in the coastal zones, (right) WaVe (WV) mode vignettes - available in the open ocean.

Not all Sentinel-1 IW acquisitions are processed into Level 2 products due to the limited capacities of the ESA Instrument Processing Facility (IPF). Therefore the required Sentinel-1 Level 2 IW OCN RVL products were generated from RAW data (Copernicus, 2017) using the following processing chain (Figure 2): (i) generate Level 1 Single Look Complex (SLC) products from the Level 0 IW RAW data using TOPSAR mode data processor based on the Engen & Larsen (2011); (ii) process the SLC products using a prototype version of the Sentinel-1 Level 2 processor (Engen & Johnsen, 2010) to get Level 2 OCN RVL products. In case of WV mode, we start the processing from the official Level 2 OCN RVL product. The calibration of the IW and WV Level 2 products and geophysical correction steps indicated in Figure 2 are further discussed in sections 2.2.2 and 2.2.3 respectively.

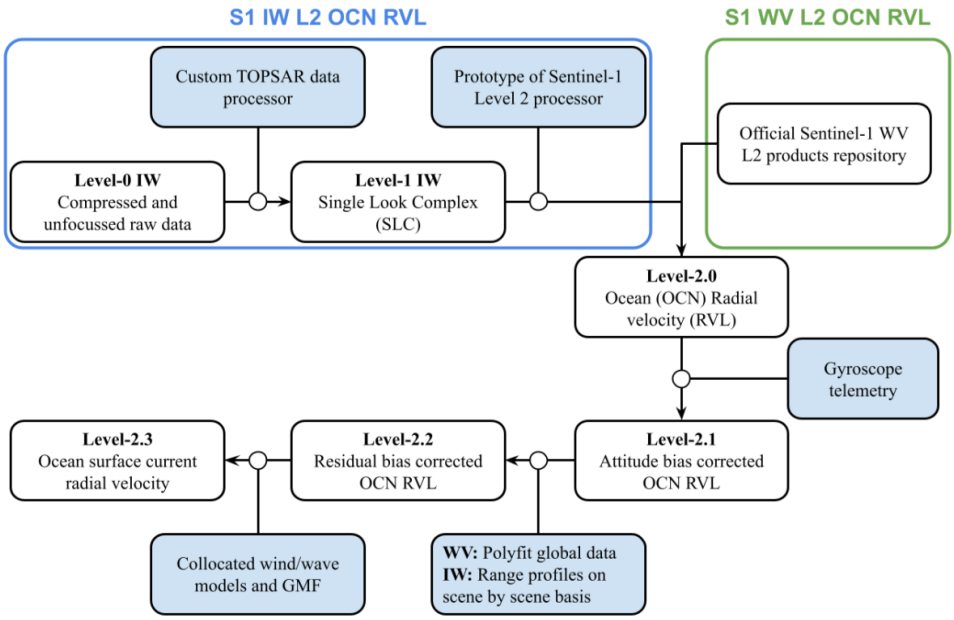

Figure 2. Flow chart illustrating the processing steps from raw data to the final ocean surface current retrieval. The upper part indicates the generation of the Sentinel-1 IW Level 2 OCN RVL products from the Level 0 RAW data (blue box) and the access to the WV Level 2 products (green box). The steps following the Level 2 production indicate calibration of the attitude contribution (Level 2.1) and residual bias (Level 2.2) and subsequent removal of the sea-state-induced contribution to the Doppler shift for retrieval of the ocean surface current radial velocity (Level 2.3).

2.2.2 Calibration of the non-geophysical contributions

The Doppler centroid frequency shift, f_{dc} from the operational Sentinel-1 RVL products contains contributions from the antenna, orbit/attitude, and geophysical motion (OceanDataLab, 2019):

$$f_{dc} = f_{bias}(\beta) + f_{att}\big(\beta, \theta_{att}(t)\big) + f_{sca} + \underbrace{(f_{osc} + f_{ss})}_{f_{rvl}} \quad (1)$$

where:

- f_{bias} is the low-frequency (period >> orbital period) signal (bias) related to antenna electronic miss-pointing and low-frequency attitude variation;
- f_{att} is the high-frequency (period << orbital period) satellite attitude variation;
- θ_{att} denotes the platform attitude roll, pitch and yaw deviations from the nominal steering at time t;
- β is the off-boresight angle
- f_{sca} is the scalloping error due to SAR antenna sweep motion in the TOPSAR acquisition mode (i.e., valid only for the IW data);
- f_{rvl} is geophysical signal related to the ocean surface radial velocity (RVL) due to the combined sea-state-induced motion, f_{ss}, and the underlying ocean surface current, f_{osc}.

All non-geophysical contributions must be estimated and removed to access the signal from the ocean surface motion (Figure 2). The f_{sca} is provided from the Sentinel-1 processor. The fast varying f_{att} can be estimated using pitch, θ_p, and yaw, θ_y, deviations from the nominal attitude (OceanDataLab, 2019) available from the gyroscope telemetry:

$$f_{att} = \frac{2\upsilon f_c}{c}\left(-\Delta\theta_y \sin\beta + \Delta\theta_p \cos\beta\right) \quad (2)$$

where υ is the satellite velocity, f_c is the SAR frequency, and the c is the speed of light. Since the expected $f_{rvl} = 0\ Hz$ over the land, residual antenna related bias then can be

derived as $f_{bias} = f_{dc} - f_{att}$. The f_{bias} approximated over the land, in turn, can be used to calibrate observations over the ocean, assuming stability of the antenna pattern over a period. This can be achieved with two different approaches, depending on the acquisition mode:

1. **IW mode:** These swaths are typically acquired in the coastal areas and Western Boundary Currents (WBC), and, as such, they contain observations of the land within the scene. Therefore, the antenna pattern can be approximated with a polynomial function using land pixels within the swath on a scene-by-scene basis.

2. **WV mode:** These vignettes are available over the open ocean and only rarely acquired over the land areas. An empirical model can be trained on all available time series of the land observations and further be used to interpolate the f_{bias} over the open ocean.

2.2.3 Ocean surface current retrievals

The geophysical Doppler shift, f_{rvl}, retrieved from the Sentinel-1 RVL products after the removal of non-geophysical signal (see section 2.2.2) can be approximated as a sum of the sea-state-induced motion, f_{ss}, and surface-current-induced motion, f_{osc} (Johannessen et al., 2008) in the radar line-of-sight direction. Hence, the sea state contribution must be carefully estimated and removed to retrieve the signal from the ocean surface current (Figure 2). Deriving an analytical formula for calculating the f_{ss} is challenging, considering the complexity and number of involved parameters associated with the wind sea and swell directional wave spectra and SAR imaging geometry. Therefore, an empirical GMF can be used to predict the f_{ss} (Mouche, 2012) for the given environmental conditions and the radar configuration. Using the Sentinel-1 f_{rvl} observations we developed the GMF (see sections 3.2 and 3.3) for estimating the f_{ss} contribution to the signal based on the wind and wave information from the collocated model forecasts. The estimates of the sea state contribution can then be used to acquire the signal due to the ocean surface current in the radar range direction as

$f_{osc} = f_{rvl} - \widehat{f_{ss}}$. The f_{osc} can then be converted to the ground range ocean surface radial velocity (Johannessen et al., 2008):

$$u_{osc} = -\frac{\pi f_{osc}}{k_e \sin\theta} \qquad (4)$$

where k_e is the electromagnetic wavenumber. By analogy with the High-Frequency radar theory (HFR) (Stewart & Joy, 1974), the depth of the Sentinel-1 sensed ocean surface current is about 0.4-0.6 cm, assuming a linear vertical shear of the horizontal ocean current velocity.

2.3 Collocated datasets

A large number of Sentinel-1 acquisitions are collocated with in-situ and remote sensing observations and numerical model forecasts (see Table 1) using the Geo-SPaaS framework and Nansat software (Korosov et al., 2016).

Table 1 Datasets

Dataset	Resolution		Region	Provider	Time period
	Temporal	Spatial			
CARTHE surface drifter trajectories	5 min.	-	Norwegian coastal zone	MET Norway	October 2017- November 2017
CODAR High-Frequency radar	1 h.	5 km.	Norwegian coastal zone	MET Norway	October 2017- November 2017
ECMWF near-surface wind field	1 h.	0.125°	Global open ocean	ECMWF	December 2017 - January 2018
MEPS near-surface wind field	1 h.	2.5 km	Norwegian coastal zone	MET Norway	October 2017- November 2017, December 2017 - January 2018
WAVEWATCHIII sea state	3 h.	0.5°	Global open ocean	IFREMER	December 2017 - January 2018
MyWaveWAM sea state	1 h.	4 km.	Norwegian coastal zone	MET Norway	October 2017- November 2017, December 2017 - January 2018
Sea Surface Temperature	8 d.	4 km.	Norwegian coastal zone	NASA OBPG	October 2017- November 2017, December 2017 - January 2018
Ocean surface current climatology	1 mth	0.25°	Global open ocean	NOAA	December 2017 - January 2018
ROMS ocean surface current	1 d.	2.5 km / 800 m	Norwegian coastal zone	MET Norway	October 2017- November 2017, December 2017 - January 2018
Bathymetry	-	0.015°	Globally & coastal zone	IHO, IOC	-

2.3.1 Ocean surface drifters

Ocean drifters follow the surface currents at predefined depth. Information from the 21 CARTHE (Consortium for Advanced Research on Transport of Hydrocarbon in the Environment) drifters (Novelli et al., 2017) deployed by the MET Norway during the Fruholmen experiment in October 2017 and tracked until 11 January 2018 was used to provide Lagrangian surface current measurements. The dataset is available in open access (The Norwegian Meteorological Institute, 2020). The CARTHE drifters are designed to follow the current in the upper 60 cm with minimal wave rectification issues and wind-induced slip velocity of no more than 0.5% of the neutral wind speed at 10 m (Novelli et al., 2017). Despite some constructional differences, the drifters show nearly identical trajectories as the CODE (Coastal Ocean Dynamics Experiment) drifters (Davis, 1985), traditionally used in studies of upper ocean circulation (Röhrs, 2015). The GPS locations with an accuracy of 10 m from each drifter were acquired every 5 min and then used to calculate the drifter velocity. Given the accuracy of the GPS locations and time-frequency of the observations, the mean uncertainty of the estimated drifter velocity is about 0.06 m.

2.3.2 High-Frequency radar

The land-based High-Frequency Radars (HFRs) are used for operational monitoring of the surface currents in the coastal zones. The CODAR SeaSonde instrument is operated by MET Norway on the Fruholmen island since May 2016. The HFR instrument uses a single transmit-receive antenna and provides hourly integrated radial velocity (RVL) observations of Eulerian surface currents within directional bands of 5° and 5 km range resolution integrated to 2.5 m depth. The long-range configuration of this radar yields spatial coverage up to 175 km offshore. The data are integrated to hourly current estimates. The HFR-measured backscatter signals result from the Bragg resonance with surface waves at half the electromagnetic wavelength, i.e., surface waves of about 33.7 m for a radar frequency of 4.453 MHz. These observations are assumed to be independent of the local roughness modulations of short wind waves, which strongly affect the SAR backscatter and Doppler shift.

2.3.3 Near-surface wind field

Assuming the Fully Developed Sea (FDS), the information about the near-surface wind speed and direction can be used to approximate the wind sea state at the time of SAR acquisition. Hence it is crucial for predicting wave-induced contribution to the Doppler frequency shift observations.

Open ocean: The ECMWF Numerical Weather Prediction (NWP) model provides wind forecasts every 3 hours on the 0.125° grid in the open ocean. The wind fields from corresponding models are routinely resampled to the Sentinel-1 WV vignette grid and delivered with standard product specification (Collecte Localisation Satellites, 2019).

Coastal zone: The high-resolution regional AROME-Arctic and MEPS models (Müller, 2017) provide hourly forecasts of the wind field at the 10 m height on a 2.5 km spatial grid in the Norwegian coastal zone. The wind forecast from the nearest hour was resampled on the corresponding Sentinel-1 IW grid. A generalized validation of the MEPS versus in-situ observations showed improved accuracy of the wind forecasts as compared to the ECMWF-IFS, especially in the areas of complex coastal topography. Wind forecasts from the AROME-Arctic are also consistent with in-situ observations in the domain of study.

In this study, all wind directions were computed to follow the meteorological convention, e.g., an angle of 0° denotes northerly wind, while an angle of 90° denotes easterly wind. The SAR-registered Doppler shift senses the range component of the moving scatterers on the ocean surface. Therefore, for analysis of the SAR Doppler shift observations, the wind directions were transformed to a coordinate system whereby the directions are defined with respect to the SAR antenna look direction as:

$$\boldsymbol{\alpha'_m = \alpha_m - \alpha_{sar} - 90°} \tag{5}$$

where α_{sar} is the satellite azimuth direction and α_m is the wind direction in degrees from true north. In the SAR coordinate system, 0° denotes the antenna look direction (line-of-sight), while 90° denotes the satellite flight direction (azimuth). Hence, 0° and 180° directions (in the meteorological convention) respectively imply upwind (i.e., the

wind blows towards the radar) and downwind (i.e., the wind blows away from the radar), while 90° and 270° represent azimuth winds (i.e., the wind blows along the satellite track).

2.3.4 Sea state

The wave information from the numerical models can be used to provide a more realistic representation of the sea state at the time of SAR acquisition compared to the fully developed sea assumption, as it accounts for the wind fetches, history as well as the presence of the swell.

Open ocean: The information about the total sea state (combined wind sea and swell) at the position of the Sentinel-1 WV acquisition was extracted from the WAVEWATCHIII (WW3) model (Tolman, 2009). The model provides the sea state forecasts every 6h at a fixed 0.5° grid.

Coastal zone: Sea state forecasts from the regional operational MyWaveWAM model (Saetra, 2016) were collocated with the Sentinel-1 IW scenes. The WyWaveWAM provides hourly forecasts of the sea state on the 4 km spatial grid. The model is forced with winds from the ECMWF and AROME. Thanks to the wave partitioning available in the model products, the sea state information was available for the wind sea and swell.

Preprocessing: The straight usage of the directional wave spectra is not practical, taking into account a large number of acquisitions. Therefore, we simplified the analysis by deriving significant wave height (H_s, m), mean wave period (T_m, sec.), and mean wave propagation direction (ψ_m, deg.) from the total spectra (i.e., without partition for wind sea and swell) from the WW3 and separately for the wind sea and swell from the MyWaveWAM for each SAR image. Thus, we consider averaged information about the ensemble of wind waves and swell corresponding to the mean wave energy at the time of SAR acquisition. Following the transformation to the SAR-based coordinate system, ψ_m^w were projected with respect to the SAR antenna look direction. The wave orbital motion was then approximated by $u = \omega_m^w H_s$, where $\omega_m^w = 1/T_m^w$ is the wave frequency in Hz.

2.3.5 Sea Surface Temperature observations

The Sea Surface Temperature (SST) acquisitions from the MODIS-Aqua sensor were collocated with the Sentinel-1 IW scenes in the Norwegian coastal zone. Frequent cloud cover in the region of study prevents the regular acquisition of high-quality snapshots. Hence we used an 8-day average mosaic of the acquisitions at a spatial resolution of 4 km (when available) to compare the alignment to the Sentinel-1 ocean surface current radial velocity maps versus the location and orientation of the SST gradients.

2.3.6 Ocean surface current

The high-resolution Regional Ocean Modelling System (ROMS) provides an hourly forecast of the ocean surface current velocity covering the Norwegian coastal zone. The ROMS is run by the MET Norway on the NorKyst grid with a spatial resolution of 0.8 km (Albretsen et al., 2011) and NorShelf grid with a resolution of 2.4 km (Röhrs, et al., 2018). The model is forced by the winds from the ECMWF, tidal forcing from the TPXO, taking into account the runoffs from the Norwegian and Swedish rivers with more information provided in the corresponding literature. We collocated daily mean ocean current velocity fields at 0 m depth from the Sentinel-1 IW acquisitions on the scene by scene basis. To study Sentinel-1 WV observations in the open ocean, we used global monthly near-surface ocean velocity climatology derived from multiyear surface drifter observations (Laurindo et al., 2017).

3. Chapter 3 – Summary of results

3.1 Paper 1 - Evaluation of radial ocean surface currents derived from Sentinel-1 IW Doppler shift using coastal radar and Lagrangian surface drifter observations

The methodology of retrieving the ocean surface current Radial VeLocities (RVLs) from the Sentinel-1 A/B Doppler shift observations have been rapidly developing since the launches of the missions in 2014/2016. The validation of the state-of-art Sentinel-1 RVL retrievals versus independent in-situ and remote sensing observations is essential for further development of the method and for operational application. In this paper, we validate the Sentinel-1 A/B L2 RVL products acquired in October - November 2017 in the Norwegian coastal zone using land-based High-Frequency Radar (HFR) and Lagrangian surface drifter observations. We also use wind, wave, and current information from the collocated numerical models in order to evaluate the signal under various environmental conditions.

We used an in-house Geo-SPaaS platform for routine collocation and reprojection of the in-situ and model data on the same grid. The analysis of the Sentinel-1 RVL fields shows that distinct patterns of the Norwegian Coastal Current (NCC) can be detected with range directed currents reaching up to 0.7 m/s (Figure 3a). Moreover, the retrieved NCC patterns agree with trajectories of the collocated in-situ CARTHE drifters and the collocated Sea Surface Temperature field (Figure 3b). Based on point by point comparison, we observe good agreement between the SAR and the drifter derived RVL with RMSD between 0.17 and 0.30 m/s and mean bias of -0.12 to 0.23 m/s. Taking into account the uncertainty (about 0.06 m/s) of drifter observations, these data provide a reliable source for validation of the SAR retrievals. The future development, therefore, would benefit from an extensive drifter campaign to ensure a larger amount of independent drifters within the collocated SAR scene in order to increase the confidence of acquired statistics.

The HFR observations are available hourly in the coastal zone yielding an opportunity for more systematic validation of the SAR data compared to the surface drifters.

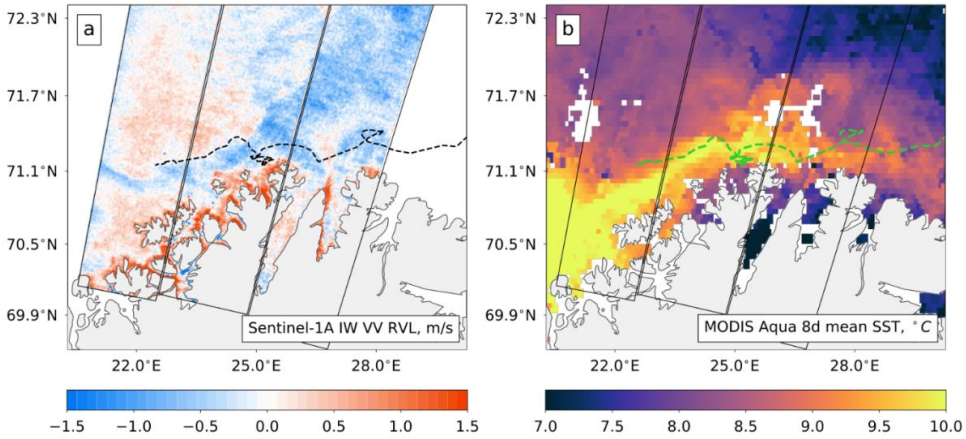

Figure 3. (a) Sentinel-1A IW RVL on 27 October 2017 05:03:26. (b) Average SST from MODIS Aqua observations (8 days, 8–16 October 2017). Black frames define SAR swath boundaries. The dashed (black and green) lines indicate the trajectory of a surface drifter between 19 and 28 October 2017.

Comparison of the Sentinel-1 derived surface currents RVLs with HFR RVLs from the co-directed beam reveals acceptable agreement with Root Mean Squared Difference (RMSD) from 0.20 to 0.29 m/s and mean bias between -0.12 and 0.12 m/s. Notably, for some scenes, the acquired statistics were unsatisfactory high due to issues with the calibration or/and the signal partitioning for sea state and current in the SAR data. The acquired RMSDs between SAR and HFR are comparable to those presented in an earlier study for the Iroise Sea (Danilo et al., 2007). We also found that the HFR observations from available instrument are rather uncertain (up to 0.25 m/s after filtering), and, hence, cannot be used as reliable ground truth for validation of the SAR-based RVL retrievals. However, the lower-range/higher-frequency HFRs should also be tested further as they provide finer spatial resolution and smaller penetration depth compared to the system installed in the northern Norwegian coastal zone.

All instruments utilized in this study provide estimates of the ocean current at <0.01, ~0.6, and ~2.5m depth, respectively, for the Sentinel-1 SAR, drifters, and the HFR. These depths will certainly be exposed to different impacts from the forcing field (e.g., wind and heat flux). The incoming solar radiation, freshwater runoff, precipitation, and mixing due to the near-surface wind and waves influence this shallow upper layer variability and thus the vertical shear of the ocean current.

Comparison of the ocean surface current derived from SAR with the ocean model simulations demonstrated a generally good consistency. Although the model does not assimilate any observations, it well reproduces main circulation features in the region. Nevertheless, some dynamical features were expectably not reproduced by the model simulations. (Sperrevik et al., 2015) demonstrated that assimilation of the RVL derived from the coastal HFR improves the model simulations (positioning of eddies and current speed). The operational Sentinel-1 A/B SAR platforms could therefore provide high spatial resolution RVL maps up to two times per day (for high-latitude regions). In light of the given spatial-temporal characteristics and accurate calibration, the SAR-based RVL retrievals could, therefore, provide valuable information for validation and assimilation in numerical ocean models.

Provided more observations are available, the approach developed in this study can be used for validation of the Sentinel-1 ocean surface current radial velocity retrievals. All in all, the estimated accuracy of Sentinel-1 retrievals is within the range of requirements for the horizontal ocean surface current velocity, according to the GlobCurrent users survey (Donlon, 2013). The artifacts associated with the calibration and geophysical signal partitioning, noted in this study, can provide a roadmap for further developments in order to improve the accuracy of the ocean surface current retrievals from the Sentinel-1 Doppler shift observations.

3.2 Paper 2 - On removal of sea state contribution to Sentinel-1 Doppler shift for retrieving Reliable Ocean surface current

In 2018, a novel approach for calibration of attitude contribution was developed based on the gyroscope telemetry available from the Sentinel-1B platform in the December 2017 - January 2018 (OceanDataLab, 2019), yielding improved accuracy of the geophysical retrievals from the Sentinel-1. In this paper, we take advantage of this calibrated Sentinel-1B WaVe (WV) mode observations to develop an empirical model function for estimating the sea state contribution to the registered geophysical Doppler

shift and, in turn, improve the accuracy of the ocean surface current Radial VeLocity (RVL) retrievals in the open ocean.

In order to evaluate the state-of-art calibration technique, we estimated that the attitude is responsible for up to 40% of the variation in observations, based on data collected over land. We found that when the attitude variation is removed, the residual signal, associated with the antenna electronic miss-pointing, is characterized by 4 Hz variation with a period of about 300 orbits. After re-calibration, the residual variation in observations does not exceed 3 Hz, corresponding to the 0.14-0.21 m/s when converted to the ground range radial velocity, depending on the incidence angle.

In order to examine the Doppler shift as a function of open ocean wind and wave fields, the Sentinel-1B acquisitions were down-selected to avoid areas of strong surface currents, coastal areas with shallow water topography, and the presence of sea ice. Assuming the Fully Developed Sea (FDS), the wave-induced radial velocity can be approximated as a function of the range-directed wind speed. We found that the wind sea contribution to the Doppler signal is generally weaker for WV2 compared to WV1

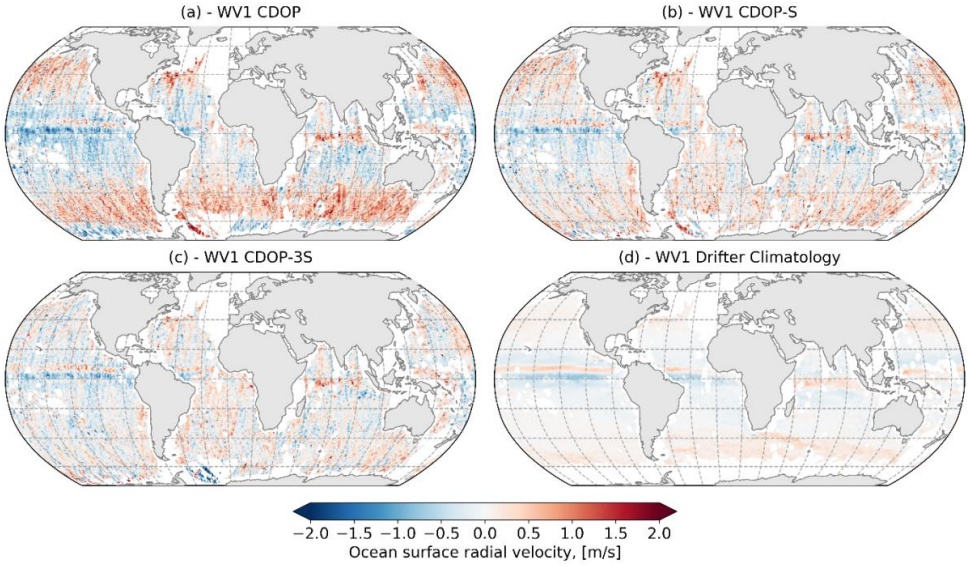

Figure 4. Gridded climatology of ocean surface current radial velocity (in m/s) based on 2 months of Sentinel-1B observations from combined ascending and descending passes. The SAR derived RVL was retrieved using CDOP (a), CDOP-S (b), and CDOP-3S (c) and compared to ocean surface drifter climatology (d). Positive (negative) values represent eastern (western flow).

for winds > 5 m/s. Notably, the ocean surface radial velocity is about 24% (12%) of the range wind speed at $\theta = 23°(\theta = 36°)$. The wind field variability, fetch limitations, and presence of swell (especially at low wind speeds, when the ocean surface wave motion is governed by remotely generated waves) add additional spread in the observed dependency. Using the WAVEWATCH III, the difference between the wave orbital velocity in range direction and the range wind speed can explain a fraction of the observed spread, especially for the WV1 data where the sea state contribution is much larger compared to the WV2 data.

The empirical CDOP model, initially developed using the historic Envisat ASAR observations (Mouche, 2012), has been used for predicting wind-wave contribution to the geophysical signal for the given wind field and radar configuration. We found that it systematically underestimates the wave contribution by up to 27% (25%) for the WV1(WV2) observations. Re-training of the model to fit the Sentinel-1 WV observations (CDOP-S), preserving physical assumptions from the CDOP, improves the accuracy of the wave contribution estimates (Figure 4b) compared to the CDOP (Figure 4a). This confirms the hypotheses that CDOP, due to its empirical nature, inherits biases from the ASAR observations, and as such, cannot be routinely applied to the Sentinel-1 observations. Utilizing established relationships between wind, waves, and Doppler observations, we developed a new GMF (CDOP-3S), which accounts for the wave period, propagation direction, and significant height in addition to the wind parameters. The CDOP-3S yields additional considerable improvements especially for the Southern Ocean and the North Pacific with (Figure 4c). This is explained by the frequent presence of storms in these ocean basins that generate swell fields and crossing seas, which, in turn, will affect the Doppler shift signals. All in all, the CDOP-3S underestimates the wave contribution by 10% (16%) with Root Mean Squared Error (RMSE) of 7.03(7.42) Hz for the WV1(WV2) observations.

Given accurate calibration and wave bias correction from the CDOP-3S, the ocean surface radial velocity map (Figure 4c) from two months of Sentinel-1B acquisitions agrees with the surface current climatology based on multiyear drifter observations (Figure 4d). As such, the Sentinel-1B Doppler shift observations from the wave mode

acquisitions reveal promising capabilities for regular monitoring of equatorial ocean surface currents for 20 km resolution cells at a monthly time scale. Reprocessing of the full Sentinel-1 A/B dataset using the novel attitude bias correction is, therefore, strongly recommended for further improvement of the GMF accuracy and subsequent regular use of the Sentinel-1 A/B for ocean surface current monitoring since the corresponding launches in 2014/2016.

3.3 Paper 3 - Towards Retrieving Reliable Ocean Surface Currents in the Coastal Zone from the Sentinel-1 Doppler Shift Observations

Building on the development and findings in Paper 2, in this paper, we use high-resolution (1.5 km) Sentinel-1B Interferometric Wide (IW) swaths from December 2017 - January 2018 collocated wind regional wind fields (MEPS) and sea state (MyWaveWAM) forecasts to improve the ocean surface current retrievals in the challenging environmental conditions along the coastal zone of northern Norway.

Analysis of IW swaths captured over the rainforests revealed that an unstable satellite attitude is responsible for up to 30% of the variation in the Doppler signal, while the changing antenna pattern can describe an additional 15%. After the re-calibration, the residual variation in observations is about 3.8 Hz, corresponding to the 0.15-0.21 m/s in the ground range radial velocity, which is consistent with the previous result for the low-resolution WV data. This indicates clear improvement compared to the 6.89 Hz residual reported in Paper 1 without the available attitude information.

The Doppler shift observations acquired under onshore and offshore wind conditions were examined under a broad range of incidence angles (compared to Paper 2) between $\theta \approx 31°$ and $\theta \approx 45°$, avoiding regions of shallow topography and strong ocean surface currents. We compared the physical dependencies estimated from the IW data with results from Paper 2 for the fixed $\theta = 36°$, assuming that the wave development in the deep water coastal zone under onshore winds is similar to the open ocean. As estimated from the IW data, the observed radial velocity increases linearly as 10% of the range wind speed for onshore directions, indicating consistency between the two

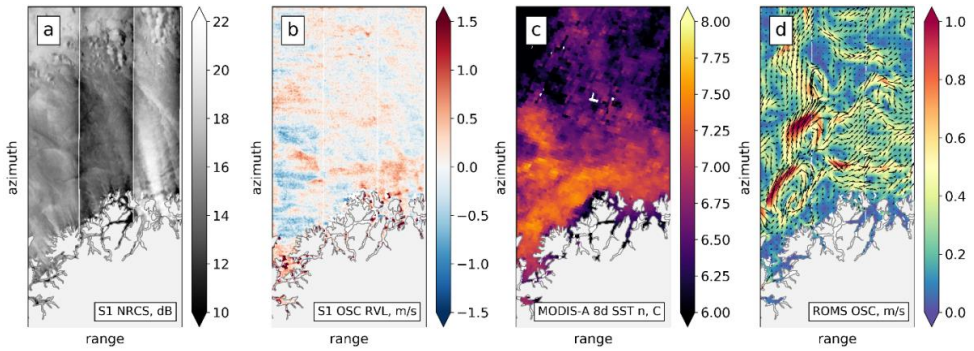

Figure 5. Ascending Sentinel-1B IW VV scene acquired in IW mode on 10 December 2017 at 16:06:07: (a) Normalized Radar Cross Section in dB; (b) Ocean surface current radial velocity derived from the Doppler observations using CDOP3Si model; (c) Night-time sea surface temperature from MODIS-Aqua averaged between 3rd and 10th December 2017; (d) Daily ocean surface current velocity from the ROMS model.

independent observation modes (WV versus IW) at $\theta = 36°$. When the wind blows offshore, the corresponding radial velocity increases at a slower rate for winds up to 8-10 m/s, which is assumed to be related to the fetch limited underdeveloped seas. The wind-wave orbital velocity, averaged from the full ensemble of wind waves, from the collocated wave model provides a better fit to the SAR observations compared to the wind field. The wave modeling accounts for the wind history and fetches and hence provides a better representation of the sea state at SAR acquisition time compare to the FDS. The swell-induced orbital velocity indicates a much weaker correlation with the SAR-derived radial velocities and provides valuable input on a scene-by-scene basis. Expanding the analysis for the full range of incidence angles indicates the strong sensitivity of the SAR radial velocity observations to the incidence angle. Notably, the impact of the swell is the most important in the near-range and not relevant in the far-range, according to estimated statistics.

Based on the established physical relationships between the Sentinel-1 IW observations and the sea state, we developed an empirical model function for predicting wave-induced contribution to the geophysical Doppler shift. The model, based only on the wind and incidence angle information (CDOPSi), underestimates sea state contribution, on average, by 18% and 30% for onshore and offshore wind directions, respectively. This difference confirmes that the wind information is not sufficient for

predicting wave contributions to the signal, as it does not provide an adequate approximation of the sea state, especially for offshore winds. The CDOP3Si model accounts for the significant wave height, mean period, and mean direction for the wind sea and swell in addition to the wind speed and direction. The accuracy of the CDOP3Si is significantly improved compared to the CDOPSi, and comparable with the results from Paper 2 for the $\theta \approx 36°$. Moreover, the CDOP3Si has comparable accuracy for onshore and offshore wind cases, showing skill in predicting the sea-state-induced contribution to the registered Doppler shift in the mixed fetch conditions of the coastal zone. Essentially, the CDOP3Si model yields much clearer ocean surface current retrievals compared to previously available in Paper 1 based on the CDOP model.

Although this study is based on two months of regional observations from the single Sentinel-1B platform, the results are promising. The Sentinel-1 IW scenes show the capacity to retrieve high-resolution patterns of the Norwegian coastal current and mesoscale eddies with radial velocities of 0.5 m/s (Figure 5). The SAR derived radial velocity maps are consistent with the surface current velocity field derived from the regional model simulation, although some features are misplaced in the model compared to observations. In addition, the SAR-derived ocean surface current patterns are also consistent with the satellite-derived sea surface temperature fields.

4. Chapter 4 – Conclusions and outlook

This thesis builds on the legacy of pioneering studies based on the Envisat ASAR mission (2002-2012), which have demonstrated the potential of using the SAR-derived Doppler frequency shift to retrieve ocean surface current radial velocities. The operational Sentinel-1 A/B C-Band SAR mission was launched in 2014/2016 to support the Copernicus Marine Environment Monitoring Service (CMEMS) program. With this mission, the range Doppler velocity retrievals have gradually become available in the operational products. However, severe non-geophysical contributions from antenna electronic miss-pointing, unstable satellite attitude, and the challenging separation of geophysical signal for the sea state and surface current contributions significantly affect the accuracy of the ocean surface current retrievals from the Sentinel-1 acquisitions.

The first paper of this thesis focuses on validating the Sentinel-1 RVL products from October-November 2017 to assess the ocean surface current retrievals in the coastal zone, compared to independent in-situ and remote sensing observations. Although in some cases, the SAR-derived surface currents are consistent with observations, we also note certain limitations due to insufficient calibration and partitioning of the geophysical signal for the sea state and current contributions.

In 2018 a novel approach (OceanDataLab, 2019) for calibration of attitude contribution to the Doppler shift was developed based on the gyroscope telemetry available for the test period in December 2017-January 2018 from the Sentinel-1B satellite. The second paper of the thesis builds on this newly calibrated dataset to develop an empirical CDOP3S model for predicting sea-state-induced contribution to the Sentinel-1 WV Doppler shift observations and, in turn, improve the accuracy of the ocean surface current retrievals. The third paper extends the study in paper 2 in order to derive ocean surface current retrievals from the high-resolution Sentinel-1 IW swaths in the more challenging environmental conditions of the coastal zone.

All in all, the results are promising, in spite of the limited availability of calibrated data. The Sentinel-1 derived ocean surface current radial velocities can be used to monitor

equatorial surface currents at a monthly timescale with a 20 km spatial resolution. Moreover, western boundary currents and coastal current features can be explored at a spatial resolution of 1-2 km on a case-by-case basis. Therefore, reprocessing the full Sentinel-1 A/B dataset using the novel attitude bias correction is strongly recommended to further improve the empirical model accuracy. The SAR-registered ocean surface roughness can also be used to retrieve information about the sea state. This observation-based sea state retrievals should, therefore, be further investigated for the correction of the sea state contribution to the Doppler shift observations, especially in regions of complex wave-current interactions. Evidently, the co-variability between the SAR-detected surface roughness and Doppler shift should be further systematically explored. Moreover, an extensive validation campaign, based on collocated in-situ wind, wave, and surface current measurements and Sentinel-1 A/B scenes, would be highly useful to demonstrate the importance of regular use of these data for ocean surface current monitoring. In anticipation of operational Sentinel-1 A/B SAR-based Doppler shift observations, the twice daily (for high-latitude regions) derived high spatial resolution RVL maps will also provide valuable information for validation and assimilation in numerical ocean models.

References

Abascal, A. J., Sanchez, J., Chiri, H., Ferrer, M. I., Cárdenas, M., Gallego, A., Castanedo, S., Medina, R., Alonso-Martirena, A., Berx, B., Turrell, W. R., & Hughes, S. L. (2017). Operational oil spill trajectory modeling using HF radar currents: A northwest European continental shelf case study. *Marine Pollution Bulletin*, *119*(1), 336–350. https://doi.org/10.1016/j.marpolbul.2017.04.010

Albretsen, J., Sperrevik, A. K., Staalstrøm, A., Sandvik, A. D., Vikebø, F., & Asplin, L. (2011). NorKyst-800 Report No. 1 User Manual and technical descriptions. *Technical Report 2, Fisken Og Havet, Institute of Marine Research*, *2*, 1–48.

Barrick, D. E., Evans, M. W., & Weber, B. L. (1977). Ocean surface currents mapped by radar. *Science*, *198*(4313), 138–144. https://doi.org/10.1126/science.198.4313.138

Breivik, Ø., Allen, A. A., Maisondieu, C., & Olagnon, M. (2013). Advances in search and rescue at sea Topical Collection on Advances in Search and Rescue at Sea. *Ocean Dynamics*, *63*(1), 83–88. https://doi.org/10.1007/s10236-012-0581-1

Chapron, B., Collard, F., & Ardhuin, F. (2005). Direct measurements of ocean surface velocity from space: Interpretation and validation. *Journal of Geophysical Research C: Oceans*, *110*(7), 1–17. https://doi.org/10.1029/2004JC002809

Copernicus. (2017). *Sentinel-1 data*. Retrieved February 1, 2018, from scihub.copernicus.eu

Dagestad, K.-F., Horstmann, J., Mouche, A., Perrie, W., Shen, H., Zhang, B., Li, X., Monaldo, F., Pichel, W., Lehner, S., & others. (2012). Wind Retrieval from Synthetic Aperture Radar - An Overview. *4th SAR Oceanography Workshop (SEASAR 2012)*, *3*, 22.

Danilo, C., Chapron, B., Mouche, A., Garello, R., & Collard, F. (2007). Comparisons between HF radar and SAR current measurements in the Iroise Sea. *OCEANS 2007 - Europe*, *July*, 1–5. https://doi.org/10.1109/OCEANSE.2007.4302424

Davis, R. E. (1985). Drifter observations of coastal surface currents during CODE: The statistical and dynamical views. *Journal of Geophysical Research*, *90*(C3), 4756. https://doi.org/10.1029/JC090iC03p04756

Donlon, C. (2013). *ESA Data User Element (DUE) GlobCurrent user requirement document (URD)* (Tech. Rep.). The Netherland: European Space Research and Technology Centre, Keplerlaan 1, 2201, AZ Noordwijk.

Engen, G., & Johnsen, H. (2010). *Sentinel-1 Doppler and Ocean Radial Velocity (RVL) Algorithm Definition (v1.2)* (Issues S1-TN-NRT-53–0658). https://sentinel.esa.int/web/sentinel/document-library/content/-/article/sentinel-1-

doppler-and-ocean-radial-velocity-rvl-algorithm-definition

Engen, G., & Larsen, Y. (2011). *Efficient Full Aperture Processing of TOPS Mode Data Using the Moving Band Chirp Z -Transform*. *49*(10), 3688–3693.

Espeseth, M. M., Jones, C. E., Holt, B., Brekke, C., & Skrunes, S. (2020). Oil-Spill-Response-Oriented Information Products Derived from a Rapid-Repeat Time Series of SAR Images. *IEEE Journal of Selected Topics in Applied Earth Observations and Remote Sensing*, *13*, 3448–3461. https://doi.org/10.1109/JSTARS.2020.3003686

Hansen, M. W., Collard, F., Dagestad, K. F., Johannessen, J. A., Fabry, P., & Chapron, B. (2011). Retrieval of sea surface range velocities from Envisat ASAR doppler centroid measurements. *IEEE Transactions on Geoscience and Remote Sensing*, *49*(10 PART 1), 3582–3592. https://doi.org/10.1109/TGRS.2011.2153864

Hansen, M. W., Johannessen, J. A., Dagestad, K. F., Collard, F., & Chapron, B. (2011). Monitoring the surface inflow of Atlantic Water to the Norwegian Sea using Envisat ASAR. *Journal of Geophysical Research*, *116*(C12), C12008. https://doi.org/10.1029/2011JC007375

Haza, A. C., D'Asaro, E., Chang, H., Chen, S., Curcic, M., Guigand, C., Huntley, H. S., Jacobs, G., Novelli, G., Özgökmen, T. M., Poje, A. C., Ryan, E., & Shcherbina, A. (2018). Drogue-loss detection for surface drifters during the Lagrangian Submesoscale Experiment (LASER). *Journal of Atmospheric and Oceanic Technology*, *35*(4), 705–725. https://doi.org/10.1175/JTECH-D-17-0143.1

Johannessen, J. A., Chapron, B., Collard, F., Kudryavtsev, V., Mouche, A., Akimov, D., & Dagestad, K. F. (2008). Direct ocean surface velocity measurements from space: Improved quantitative interpretation of Envisat ASAR observations. *Geophysical Research Letters*, *35*(22), 1–6. https://doi.org/10.1029/2008GL035709

Johannessen, J. A., Raj, R. P., Nilsen, J. E. Ø., Pripp, T., Knudsen, P., Counillon, F., Stammer, D., Bertino, L., Andersen, O. B., Serra, N., & Koldunov, N. (2014). Toward Improved Estimation of the Dynamic Topography and Ocean Circulation in the High Latitude and Arctic Ocean: The Importance of GOCE. *Surveys in Geophysics*, *35*(3), 661–679. https://doi.org/10.1007/s10712-013-9270-y

Johansson, A. M., Espeseth, M. M., Brekke, C., & Holt, B. (2020). Can Mineral Oil Slicks Be Distinguished from Newly Formed Sea Ice Using Synthetic Aperture Radar? *IEEE Journal of Selected Topics in Applied Earth Observations and Remote Sensing*, *13*, 4996–5010. https://doi.org/10.1109/JSTARS.2020.3017278

Korosov, A., Hansen, M. W., Dagestad, K., Yamakawa, A., Vines, A., & Riechert,

M. (2016). Nansat: a Scientist-Orientated Python Package for Geospatial Data Processing. *Journal of Open Research Software*, *4*. https://doi.org/10.5334/jors.120

Korosov, A., Rampal, P., Toudal Pedersen, L., Saldo, R., Ye, Y., Heygster, G., Lavergne, T., Aaboe, S., & Girard-Ardhuin, F. (2018). A new tracking algorithm for sea ice age distribution estimation. *Cryosphere*, *12*(6), 2073–2085. https://doi.org/10.5194/tc-12-2073-2018

Laurindo, L. C., Mariano, A. J., & Lumpkin, R. (2017). An improved near-surface velocity climatology for the global ocean from drifter observations. *Deep-Sea Research Part I: Oceanographic Research Papers*, *124*(3), 73–92. https://doi.org/10.1016/j.dsr.2017.04.009

Le Traon, P.-Y., Antoine, D., Bentamy, A., Bonekamp, H., Breivik, L. A., Chapron, B., Corlett, G., Dibarboure, G., DiGiacomo, P., Donlon, C., Faugère, Y., Font, J., Girard-Ardhuin, F., Gohin, F., Johannessen, J. A., Kamachi, M., Lagerloef, G., Lambin, J., Larnicol, G., … Wilkin, J. (2015). Use of satellite observations for operational oceanography: recent achievements and future prospects. *Journal of Operational Oceanography*, *8*(sup1), s12–s27. https://doi.org/10.1080/1755876X.2015.1022050

Lohse, J., Doulgeris, A. P., Dierking, W., & Dierking, W. (2020). Mapping sea-ice types from Sentinel-1 considering the surface-type dependent effect of incidence angle. *Annals of Glaciology*, 1–11. https://doi.org/10.1017/aog.2020.45

Lumpkin, R., & Johnson, G. C. (2013). Global ocean surface velocities from drifters: Mean, variance, El Niño-Southern Oscillation response, and seasonal cycle. *Journal of Geophysical Research: Oceans*, *118*(6), 2992–3006. https://doi.org/10.1002/jgrc.20210

Maximenko, N., Lumpkin, R., & Centurioni, L. (2013). Ocean surface circulation. *International Geophysics*, *103*, 283–304. https://doi.org/10.1016/B978-0-12-391851-2.00012-X

Mouche, A. A., Collard, F., Chapron, B., Dagestad, K. F., Guitton, G., Johannessen, J. A., Kerbaol, V., & Hansen, M. W. (2012). On the use of Doppler shift for sea surface wind retrieval from SAR. *IEEE Transactions on Geoscience and Remote Sensing*, *50*(7 PART 2), 2901–2909. https://doi.org/10.1109/TGRS.2011.2174998

Nilsen, V., Engen, G., & Johnsen, H. (2019). A novel approach to SAR ocean wind retrieval. *IEEE Transactions on Geoscience and Remote Sensing*, *57*(9), 6986–6995. https://doi.org/10.1109/TGRS.2019.2909838

Novelli, G., Guigand, C. M., Cousin, C., Ryan, E. H., Laxague, N. J. M., Dai, H., Haus, B. K., & özgökmen, T. M. (2017). A biodegradable surface drifter for ocean sampling on a massive scale. *Journal of Atmospheric and Oceanic*

Technology, *34*(11), 2509–2532. https://doi.org/10.1175/JTECH-D-17-0055.1

OceanDataLab. (2019). S-1 RVL DIL4: Algorithm description document. ESRIN: ESA.

Romeiser, R., & Thompson, D. R. (2000). Numerical study on the along-track interferometric radar imaging mechanism of oceanic surface currents. *IEEE Transactions on Geoscience and Remote Sensing*, *38*(1 II), 446–458. https://doi.org/10.1109/36.823940

Rouault, M. J., Mouche, A., Collard, F., Johannessen, J. A., & Chapron, B. (2010). *Mapping the Agulhas Current from space : An assessment of ASAR surface current velocities*. *115*(June), 1–14. https://doi.org/10.1029/2009JC006050

Sperrevik, A. K., Christensen, K. H., & Röhrs, J. (2015). Constraining energetic slope currents through assimilation of high-frequency radar observations. *Ocean Science*, *11*(2), 237–249. https://doi.org/10.5194/os-11-237-2015

Stewart, R. H., & Joy, J. W. (1974). HF radio measurements of surface currents. *Deep-Sea Research and Oceanographic Abstracts*, *21*(12), 1039–1049. https://doi.org/10.1016/0011-7471(74)90066-7

Stopa, J. E., Mouche, A. A., Chapron, B., & Collard, F. (2017). Sea State Impacts on Wind Speed Retrievals from C-Band Radars. *IEEE Journal of Selected Topics in Applied Earth Observations and Remote Sensing*, *10*(5), 2147–2155. https://doi.org/10.1109/JSTARS.2016.2609101

Tolman, H. L. (2009). *User manual and system documentation of WAVEWATCH III TM version 3.14 †*.

Zakhvatkina, N., Smirnov, V., & Bychkova, I. (2019). Satellite SAR Data-based Sea Ice Classification: An Overview. *Geosciences*, *9*(4), 152. https://doi.org/10.3390/geosciences9040152

JGR Oceans

RESEARCH ARTICLE
10.1029/2019JC015743

Evaluation of Radial Ocean Surface Currents Derived From Sentinel-1 IW Doppler Shift Using Coastal Radar and Lagrangian Surface Drifter Observations

A. Moiseev[1], H. Johnsen[2], M. W. Hansen[1,3], and J. A. Johannessen[1,4]

[1]Nansen Environmental and Remote Sensing Center, Bergen, Norway, [2]NORCE Norwegian Research Center AS, Tromso, Norway, [3]Norwegian Meteorological Institute, Bergen, Norway, [4]Geophysical Institute, University of Bergen, Bergen, Norway

Key Points:
- Radial velocities from Sentinel-1 were evaluated using HF-radar and ocean surface drifter observations
- Sentinel-1 RVLs can be used to provide a reliable observations of the ocean surface currents in the coastal zone
- The sea state contribution to the SAR Doppler shift must be taken into account in the wind-wave bias correction

Supporting Information:
- Data Set S1
- Data Set S2

Correspondence to:
A. Moiseev,
artem.moiseev@nersc.no

Citation:
Moiseev, A., Johnsen, H., Hansen, M. W., & Johannessen, J. A. (2020). Evaluation of radial ocean surface currents derived from Sentinel-1 IW Doppler shift using coastal radar and Lagrangian surface drifter observations. *Journal of Geophysical Research: Oceans*, *125*, e2019JC015743. https://doi.org/10.1029/2019JC015743

Received 10 OCT 2019
Accepted 9 MAR 2020
Accepted article online 20 MAR 2020

Abstract Ocean surface radial velocities (RVLs) derived from the Sentinel-1 A/B Interferomic Wide (IW) mode Doppler frequency shift observations are regularly acquired over the Norwegian coastal zone. These data can be used to complement existing ocean observation systems with high-resolution (up to 1.5 × 1.5 km) spatial ocean surface current (OSC) maps. In this study, Sentinel-1 IW Level 2 OSC retrievals were obtained from 2 months (October–November 2017) of raw Doppler shift observations acquired over the Norwegian Coastal Current (NCC). The results were evaluated using coastal high-frequency radar (HFR) and Lagrangian ocean surface drifter observations. The analysis shows that distinct patterns of the NCC, with range directed currents reaching up to 0.7 m/s, can be detected in the SAR data. The mean bias between Synthetic Aperture Radar (SAR) and HFR observations was −0.08 m/s and the root mean square deviation (RMSD) was 0.25 m/s. In comparison, the agreement between the SAR-derived OSC and the trajectories from Lagrangian surface drifters showed a mean bias of 0.02 m/s and an RMSD of 0.24 m/s. The accuracy of the SAR OSC retrievals rely on precise wind-wave bias correction. Hence, the accuracy of the model wind field (speed and direction) is crucial. The sea state contribution must also be taken into account during the bias correction. A typical required accuracy of the OSC velocity is on the order of 0.1 m/s. Therefore, the comparisons demonstrate that the use of SAR for OSC retrieval is promising.

Plain Language Summary Knowledge of ocean surface currents is crucial for tracking oil spills and marine debris (e.g., plastic), search and rescue operations, and fisheries. Traditionally, surface currents are studied using shipboard measurements or trajectory of buoys drifting within the water flow. Despite their accuracy, these measurements are also costly to collect and therefore irregular in time and space. The Doppler shift recorded by a radar placed on board of a satellite can be used for providing systematic snapshots of surface currents over vast areas of the ocean. However, these observations must be evaluated before application. In this study, we evaluated observations of the Norwegian Coastal Current acquired by the Sentinel-1 satellite in October–November 2017. Satellite observations were compared with collocated coastal radar and ocean surface drifters data. The analysis shows that distinct patterns of the surface current can be systematically detected in the Sentinel-1 data. The accuracy of the observations is within the range of user requirements. We underlined the importance of accurate information about wind field and ocean waves for analysis of the radar observation. The performed study demonstrates that the use of Sentinel-1 observations for the ocean surface current retrieval is promising.

1. Introduction

The global ocean circulation is responsible for a significant transport of heat and salt and plays a major role for climate and weather. Knowledge of surface currents is moreover crucial for oil spills and marine debris tracking, search and rescue operations, fish egg and larvae drift, and fisheries. In addition, surface currents affect the steepness of surface waves and are therefore also highly needed for providing reliable sea state forecasts for maritime operations and ship routing.

Ocean currents in the surface layer are composed of different contributing sources such as geostrophic current, Ekman current (Ekman, 1905), wave-induced Stokes drift (Stokes, 1880), inertial motion, and tidal

current. Direct measurement of near surface current include in situ observations from sensors located on autonomous drifting buoys and moorings as well as from shipboard measurements. These data have limited coverage but usually represent a reference for validation of satellite-based current observations and ocean models.

A large number of extensive campaigns (e.g., Global Drifter Program and Grand Lagrangian Deployment) have been initiated for mapping large-scale (about 100–200 km) (Lumpkin & Johnson, 2013; Maximenko et al., 2013) mesoscale (30–100 km) (e.g, Lumpkin & Flamant, 2013), and submesoscale (<30 km; e.g., the Lgrangian Submesoscale Experiment; Haza et al., 2018) ocean circulation with Lagrangian surface drifters. Information from these drifters are routinely used for calibration and validation of high-frequency radar (HFR; e.g., Röhrs & Christensen, 2015; Rypina et al., 2014) and satellite observations (e.g., Danielson et al., 2018; Lagerloef et al., 1999; Niiler et al., 2003; Rio et al., 2014). In addition, Lebedev et al. (2007) demonstrated that information from autonomous profiling floats (i.e., Argo) could be used for estimating mean velocity fields at the sea surface as well as in the deep ocean.

Over the last few decades, several remote sensing techniques have been developed in complement to in situ measurements. This has improved the spatial coverage of surface current observations. Land-based HFRs, for instance, have been proved useful for real-time monitoring of surface currents in the coastal zones. The HFR exploits the Doppler shift in Bragg backscatter from the ocean surface waves (Barrick et al., 1977). Attractive spatial and temporal resolution (around 3–6 km and 1 hr) and spatial coverage (up to 220 km) make these observations essential for time-critical operations such as oil spill tracking (Abascal et al., 2017) and search-and-rescue operations (Breivik et al., 2013). These HFR-based surface current observations can also be assimilated in ocean circulation models (e.g., Sperrevik et al., 2015).

Presently, satellite remote sensing observations of ocean surface currents are predominantly provided by radar altimetry (e.g., Le Traon et al., 2015; Shutler et al., 2015), whereby the sea surface height (SSH) slope is used to determine the ocean dynamic topography and the surface geostrophic ocean currents (Johannessen et al., 2014; Raj et al., 2018). The altimetry-based method provides global ocean coverage every 10 days at about 25 km spatial resolution. A range of products based on combined use of altimeter- based geostrophic current, Ekman current, Stokes drift, and surface drifter observations are available (e.g., GlobCurrent Team, 2015) and OSCAR (Bonjean & Lagerloef, 2002). However, these products are not applicable to surface current retrievals in coastal zones.

The phase information in the backscatter acquired by Synthetic Aperture Radar (SAR) can also be used to derive estimates of ocean surface currents, as demonstrated in regions of strong boundary currents (Chapron et al., 2005; Johannessen et al., 2008; Rouault et al., 2010) with typical speed above 2 m/s. The method has also been applied in weaker current regimes (about 30 to 50 cm/s) in the Nordic Seas (e.g., Hansen et al., 2011, 2012, 2013).

The Sentinel-1 C-band SAR mission includes two platforms (A and B) operated by the European Space Agency (ESA) within the Copernicus programme. Observations from Sentinel-1 A/B Interferometric Wide (IW) mode are regularly available over the Norwegian coastal zones. In this study, the ocean surface velocity retrievals from Sentinel-1 IW VV polarization Doppler frequency shift is evaluated and compared with respect to HFR and Lagrangian surface drifter observations along the Norwegian Coastal Current (NCC) at the entrance to the Barents Sea (Figure 1) over a 2-month observation period in 2017. The data and methods are presented in section 2. Results of the evaluation of the SAR observations are addressed in section 3. Section 4 contains analysis and discussion of the SAR-based ocean surface current retrieval accuracy, and possible limitations. The conclusion is provided in section 5.

2. Data and Methods

2.1. SAR Doppler Frequency Shift

A total number of 21 Sentinel-1 IW Level 2 surface Radial Velocity (RVL) products (Copernicus, 2017; Vincent et al., 2018) acquired along the coast of Norway at the entrance to the Barents Sea (Figure 1) in October and November 2017 were routinely processed. The processing procedure (Figure 2) included generation of internal Level 1 Single Look Complex (SLC) products using an in-house TOPS mode data processor (Engen & Larsen, 2011). The SLC products were then processed using a prototype version of the Sentinel-1 Level 2 processor (Engen & Johnsen, 2010) to get RVL products. The spatial resolution of the final products was about 1.5 × 1.5 km across a swath of 250 km at incidence angles in the range from 29.1° to 43.1°.

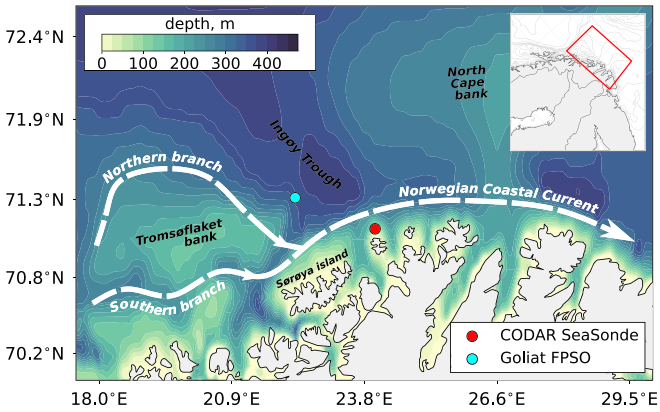

Figure 1. Bathymetric map (ETOPO5; see Edwards, 1989) and the general structure of the Norwegian Coastal Current in the study area along the northern coast of Norway and in the Barents sea. The circulation scheme is based on combined information from Sætre (2007) and Skagseth et al. (2011).

The Doppler shift estimated from the SLC data (f_{total}) contains contributions from several terms:

$$f_{total} = \underbrace{(f_{osc} + f_{ww})}_{f_{phys}} + f_{geom} + f_{elec} + \Delta f, \tag{1}$$

where f_{phys} is the geophysical term, including contributions from wind-waves (f_{ww}) and ocean surface current (f_{osc}); f_{geom} is the geometrical term; f_{elec} is the antenna electronic mispointing; and Δf is the residual error due to inaccurate estimation of the nongeophysical terms and unknown biases. All nongeophysical terms of equation (1) must be carefully estimated and removed in order to derive a reliable geophysical Doppler shift and, consequently, ocean surface current estimates. The Sentinel-1 Level 2 processor computes the f_{geom} and the f_{elec} terms from the down-linked quaternions and the antenna model, respectively (Engen & Johnsen, 2010). However, these computed terms do not correctly represent the nongeophysical Doppler shift variations, as observed in data over land areas (see Figure 3; Figure 2 in Johnsen et al., 2016).

Employing these computed terms for estimation of f_{phys} thus results in significant residual biases in both the azimuth and range directions. However, f_{geom}, f_{elec}, and Δf can be estimated using land cover data within each individual scene (Johnsen et al., 2016). Based on the assumption that the mean Doppler shift over land (f_{land}) should be 0 Hz, the nongeophysical parameters were approximated as $\overline{f}_{land} \approx f_{geom} + f_{elec} + \Delta f$, such that

$$f_{phys} = f_{total} - \overline{f}_{land}. \tag{2}$$

The geophysical Doppler frequency shift results from the Bragg resonant sea-state conditions via the projected motions of slightly rough facets, and the line-of-sight velocities of specular points and breaking wave crests, as well as the surface current (Hansen et al., 2012). For the given transmitting wavelength, λ_t, and

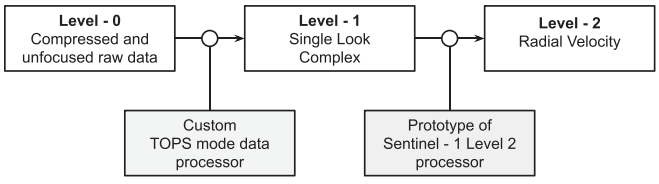

Figure 2. Processing of Sentinel-1 Interferometric Wide mode acquisitions from raw data to Level 2 RVL products.

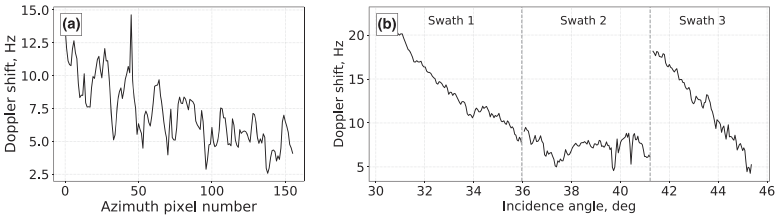

Figure 3. Mean Doppler frequency shift over land (after removing f_{geom},f_{elec} provided in data) from Sentinel-1A scene acquired on 22 October 2017 at 4:55: (a) Azimuthal direction (only 1st swath); (b) Range direction (all swaths). Pixel resolution is 1.5x1.5 km.

incidence angle, θ, the resulting ocean surface wavelength yielding the Bragg resonance conditions can be estimated as

$$\lambda_b = \frac{\lambda_t}{2\sin\theta}. \tag{3}$$

Given that transmitting frequency for the Sentinel-1 is 5.405 GHz, we can estimate that $\lambda_t \approx 5.5$ cm. Hence, from equation (3), we find that the Sentinel-1 Doppler shift acquisitions are sensitive to the wavelengths of 6–7 cm depending on the incidence angle. These short Bragg-scale waves are formed in response to the wind stress. Hereinafter, the Doppler shift resulting from wind waves is estimated and used as an approximation to the sea state contribution (i.e., the swell is ignored).

The OSC is a combination of various surface current components including, for example, the wind friction-induced Ekman flow, the geostrophic current, the wave induced Stokes drift, and tidal current. In order to retrieve the total Ocean Surface Current (OSC) from the SAR geophysical Doppler shift, the wind-wave bias (f_{ww}) must be precisely estimated and removed. The Doppler shift resulting from the OSC thus reads

$$f_{osc} \approx f_{phys} - f_{ww}. \tag{4}$$

To estimate the wind-wave bias, an empirical geophysical model function (GMF) called CDOP was proposed by Mouche et al. (2012). The model is a three-layer neural network relating the wind-dependent Envisat Advanced Synthetic Aperture Radar (ASAR) Doppler shift, incidence angle (θ) and polarization (p) at C-band to the wind speed (u_{10}), and direction (ϕ) at 10 m height from the European Centre for Medium-Range Weather Forecasts (ECMWF). Thus, the Doppler frequency shift resulting from the ocean surface current can be expressed as

$$f_{osc} = f_{phys} - f_{CDOP}(u_{10}, \phi, \theta, p). \tag{5}$$

This Doppler shift can then be converted to the radial surface current velocity:

$$V_{osc} = -\frac{\pi \cdot f_{osc}}{k_e \cdot \sin(\theta)}, \tag{6}$$

where k_e is the radar wave number. By analog with the HFR theory (Stewart & Joy, 1974) assuming the linear vertical share of the horizontal ocean current velocity, we can estimate the depth of observations as

$$d = \frac{\lambda_b}{4\pi}. \tag{7}$$

Hence, the depth of the OSC retrieved from Sentinel-1 SAR is about 0.4–0.6 cm depending on the incidence angle.

The wind-wave bias is in this study obtained by employing the CDOP model with wind information derived from the AROME-Arctic high-resolution regional Numerical Weather Prediction (NWP) model (Müller et al., 2017). Following the wind-wave bias correction (equation (5)), the resulting OSC RVL is evaluated in comparison to HFR current measurements; Lagrangian surface drifters observations; satellite Sea Surface Temperature (SST) retrievals; and the regional operational ocean circulation model (ROMS) from the Norwegian Meteorological Institute (MET Norway). These data sets are briefly presented in the following subsections.

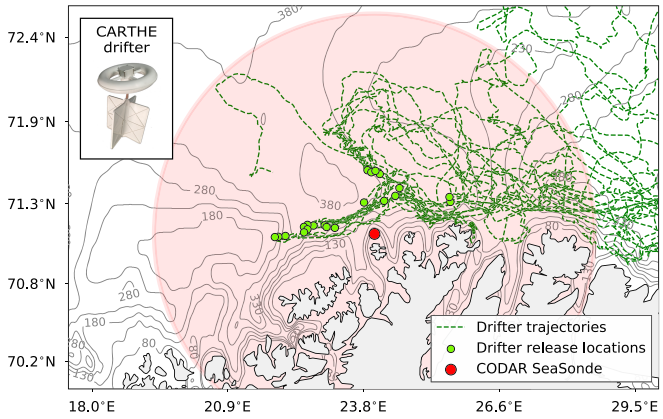

Figure 4. Trajectories from 21 CARTHE drifters acquired between October 2017 and January 2018 in the domain of study. The red marker indicates location of the CODAR SeaSonde HFR with corresponding coverage area (red shade).

2.2. High-Frequency Radar

The CODAR SeaSonde HFR instrument is operated by MET Norway on the Fruholmen island (Figure 1) since May 2016. The HFR instrument uses single transmit-receive antenna and provides hourly integrated RVL observations of Eulerian surface currents within directional bands of 5° and 5 km range resolution (The Norwegian Meteorological Institute (2016), CC 4.0 BY license). The coverage reaches up to 175 km offshore (Figure 4). The data are integrated to hourly current estimates. Uncertainties in both the spatial and temporal dimensions are provided in the data set. In this study, we use the mean of these two values for the total uncertainty. The HFR-based Bragg backscatter is derived from surface waves at a radar frequency of 4.453 MHz, which is equivalent to a wavelength of about 30 m (see equation (3)). These observations are assumed to be independent from the local roughness modulations of short wind waves, which strongly affect the SAR backscatter and Doppler shift. From equation (7) the depth of the HFR observations is estimated to about 2.5 m.

2.3. Lagrangian Surface Drifters

Information from the 21 CARTHE (Consortium for Advanced Research on Transport of Hydrocarbon in the Environment) drifters was used to complement the study with Lagrangian surface current measurements. The drifters were deployed during the Fruholmen experiment in October 2017 and tracked until 11 January 2018 (Figure 4). The CARTHE drifters are designed to follow the current in the upper 60 cm with minimal wave rectification issues and wind-induced slip velocity of no more than 0.5% of the neutral wind speed at 10 m (Novelli et al., 2017). Despite some constructional differences, the drifters show nearly identical trajectories as the Coastal Ocean Dynamics Experiment (CODE) drifters (Davis, 1985), traditionally used in studies of upper ocean circulation (e.g., Röhrs & Christensen, 2015).

Timestamps and GPS locations of the drifters were acquired every 5 min and then used to calculate the drifter velocity. In cases when the signal from a drifter was lost for more than 5 min, the observational point was eliminated. Taking into account the accuracy of the GPS locations (about 10 m accuracy) and given time frequency of the observations, the mean uncertainty of the estimated drifter velocity is about 0.06 m/s.

2.4. Sea Surface Temperature

Frequent cloud cover in the study region prevent regular acquisition of high-quality snapshots of the Sea Surface Temperature (SST) field from MODIS-Aqua. Hence, 8-day averages of Level 3 SST products (NASA Goddard Space Flight Center, 2014) were routinely acquired for comparison of the alignment to the Sentinel-1 RVL maps versus the location and orientation of the SST gradients.

2.5. AROME-Arctic Model

The AROME-Arctic high-resolution regional NWP model (Müller et al., 2017) simulations are provided by MET Norway. Hourly predictions of the near-surface wind speed and direction are openly available

(The Norwegian Meteorological Institute (2015), CC 4.0 BY license) on a 2.5 by 2.5 km grid from November 2015. As such, the time gap between the NWP forecasts and SAR acquisitions did not exceed 30 min.

The accuracy of the wind-wave bias estimation strongly relies on the quality of the available wind information. In order to evaluate the NWP model predictions, in situ observations (also provided by MET Norway) from a coastal station (Fruholmen island, close to the HFR location, Figure 1) and in the open sea (Goliat FPSO platform) were collocated with the NWP model output. Generally, the model simulations show a good agreement with the in situ wind observations. For the Goliat station the estimated Root Mean Square Deviations (RMSDs) are 1.58 and 1.96 m/s for the meridional and zonal components, respectively. In comparison, the RMSDs are about 3.6 m/s for both wind components at the Fruholmen station. These higher RMSD estimates are assumed to be related to the strong influence of the local topography on the wind field in the coastal zone, which is not properly incorporated in the 2.5 × 2.5 km model grid. These findings are consistent with the results of a more general model validation study by Müller et al. (2017).

2.6. Wave Model

Information about the significant wind wave height, period, and propagation direction were acquired from the regional operational wave forecast model, WAM (MET Norway). The hourly 4 km spatial resolution WAM forecasts are openly available via the MET Norway Thredds Service (The Norwegian Meteorological Institute, 2016, CC 4.0 BY license). The time gap between the WAM forecasts and Sentinel-1 acquisitions did not exceed 30 min.

2.7. Ocean Model

Simulated ocean surface current field was derived from the high resolution operational ocean model ROMS (MET Norway) covering the Norwegian coastal zone with 800 m grid spacing (Albretsen, 2011). The model is a 3-D free-surface, hydrostatic, primitive equation ocean model using terrain-following s coordinates in the vertical. It is a free run model (i.e., does not include any observations). An external atmospheric forcing in the model is provided from ERA-Interim archive of global atmospheric reanalysis and Hirlam hindcast database (NORA10). The model utilizes surface analysis of wind, temperature, pressure, humidity, and cloud cover four times a day (00, 06, 12, and 18 UTC) and surface forecast of accumulated precipitation and radiation twice a day. Information along open boundaries is taken from operational model MI-POM (MET Norway) and monthly mean ROMS hindcast between 1989 and 2008 (Institute of Marine Research) at 4 × km grid. The tidal forcing is based on global inverse barotropic model of ocean tides, TPXO7.26 with horizontal resolution of 0.25°. The river runoffs is based on modeled discharge from the the Norwegian and Swedish rivers (daily values). The daily average model forecasts are provided at 17 vertical z levels starting from 0 m (used in this study) and are also openly available via the MET Norway Thredds Service (The Norwegian Meteorological Institute, 2012, CC 4.0 BY license). For more details, see Albretsen (2011).

2.8. Data Discovery and Collocation

Precise collocation in time and space of the data from the different sources is crucial for reliable validation. The Geo-SPaaS (Hansen et al., 2019) framework was used for managing the geospatial data employed in the study. This allows the generation of a uniform metadata catalog and provides a Python interface for data access and analysis. The 2-D geospatial data products (i.e., SAR, SST, AROME-Arctic, WAM, and ROMS) are provided at different projections and were adjusted to a common grid using the Nansat software (Korosov et al., 2016, 2019).

For estimation of the wind-wave bias, the SAR acquisitions were collocated with the near-surface wind speed and direction from the AROME-Arctic model. The wind-wave bias was then estimated with CDOP, and subtracted from the total geophysical Doppler shift (equation (5)). The horizontal radial component of the ocean surface current was then obtained (equation (6)) and compared to the other observations.

3. Results

Following the RVL, the standard deviation of the Sentinel-1A/B IW radial Doppler shift over land was estimated to be 6.89 Hz. This corresponds to a horizontal surface velocity ranging from 0.37 to 0.29 m/s at 29° to 43° incidence angle.

Retrieval of reliable RVLs depends on a range of time varying geophysical and nongeophysical factors such as the wind-wave bias and uncertainties in the orbit and attitude control. Each SAR scene is a snapshot of a particular wind field, sea state, and ocean surface current. The accuracy of the retrievals therefore depends

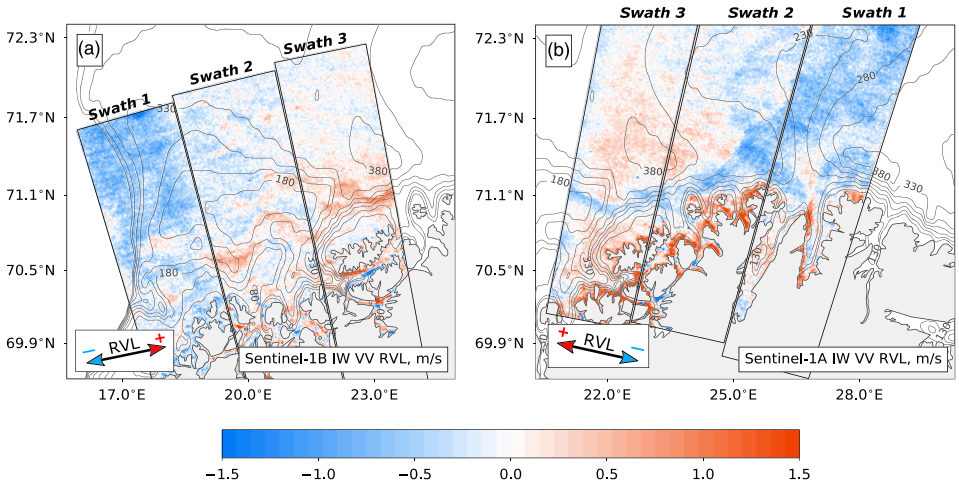

Figure 5. Maps of ocean surface radial velocity (color) at a spatial resolution of 1.5 × 1.5 km derived from (a) Sentinel-1B ascending pass acquired on 30 October 2017 15:58:51; (b) Sentinel-1A descending pass acquired on 27 October 2017 05:03:26. The color scale marks the surface velocity in m/s. The difference between positive (a) and negative (b) RVL retrievals is related to the detected current direction relative to the SAR antenna range pointing direction, which is determined by the satellite pass. Contour lines represent the bathymetry (every 50 m).

on the ability to properly quantify these three distinct contributing components, which varies in relation to the weather conditions and imaging geometry. For instance, if the wind blows parallel or near-parallel to the SAR azimuth direction (i.e., wind-wave contribution close to 0 Hz), minor uncertainties in the mode predicted wind direction can cause range oriented wind components that may yield wind-wave bias estimates of wrong sign. This, in turn, may result in increased error instead of the intended correction. In the following, the analysis is therefore limited to only single SAR scenes instead of a global comparison between the SAR retrievals and the reference data.

For each SAR scene the collocated pixels were assessed in light of the wind field (speed and direction), sea state (significant wind wave height, length, and propagation direction), geographical location (distance from the coast, water depth), and characteristics of the acquisitions (i.e., SAR swath, incidence angle, and HFR beam). Note that swell and wave-current induced wave modulations were not considered due to lack of reliable information and relatively small size of the available data set. Each of the SAR scenes was also visually inspected in order to detect cases where the Doppler calibration and/or wind-wave bias correction evidently failed.

3.1. The NCC From SAR

A narrow 10–20 km wide meandering pattern of the NCC, flowing northeastward at a speed of up to 0.7 m/s, is detected in most of the corrected SAR scenes, as demonstrated in Figure 5. As the RVL retrievals are referenced to the orientation of the satellite overpass, the ascending (red pattern in Figure 5a) and descending (blue pattern in Figure 5b) passes are both displaying the NCC with a mean flow direction toward northeast.

After the separation at the Tromsø flaket bank (see Figure 1), the NCC may typically follow two different paths (Sætre, 2007; Skagseth et al., 2011). First, it may be steered around the northern edge of the Tromsø flaket bank toward ~22°E where it merges with the nearshore branch as depicted in the descending pass shown in Figure 5b. Second, it may be steered through a trench in the bathymetry as captured in the surface RVL field retrieved from the Sentinel-1B ascending pass acquired on 30 October 2017 (Figure 5a). Intensification of the northern and southern branches is related to the prevailing wind field conditions and the corresponding Ekman transport (Sætre, 2007).

According to estimates provided by (Sætre, 2007) based on surface drifter observations, the surface velocity in the NCC is usually larger than 0.6 m/s between 69°N and 71°N. This is consistent with the RVL of the NCC (~0.7 m/s) derived from the SAR Doppler shift. Moreover, Skagseth et al. (2011) obtained a mean

current of 0.42 m/s at a depth of 24–44 m from 1 year (July 2007 to July 2008) of moored Acoustic Doppler Current Profiler observations (deployed at 70.1°N , 24°E) with a fall to winter intensification of approximately 0.1 m/s. Assuming a baroclinic structure in the velocity profile toward the surface, this also tends to acceptably compare to the RVL retrievals.

The geometry of the SAR acquisitions plays a significant role in the detection and analysis of the ocean surface currents. In particular, surface currents directed along the SAR range plane are more favorable than currents oriented along the azimuth plane. A meandering pattern of the NCC will therefore induce variations in the RVL. When the current flow becomes parallel to the SAR azimuth direction (such as in regions 70.8°N, 20.5°E, and 70.6°N, 22°E in Figure 5a), it appears to be weaker compared to regions *where*) the NCC is aligned in the range direction (such as 70.5°N, 20°E, and 71°N, 23°E in Figure 5a). Similarly, the northern branch of the NCC, which is directed toward southeast, is more clearly depicted in the RVL field acquired in the descending SAR pass. Similarly, the nearshore branch is evidently more visible in the ascending pass.

The contribution from the short and slow-moving Bragg waves (typically associated with local wind modification) to the backscatter increases with increasing incidence angle (Mouche et al., 2012). The SAR-based RVL retrieval, moreover, also depends on the incidence angle. Since $\frac{dv}{d\theta} < 0$ (where v is the range velocity and θ the incidence angle) from a simple geometrical consideration, the wind-wave induced range Doppler shift decreases with increasing incidence angle (Mouche et al., 2012; Yurovsky et al., 2019). As such, the Doppler shift resulting from the surface current may be more prominent in far range.

A range-directed decrease in the RVL field in an area of uniform wind is thus expectedly related to the incidence angle. This can be observed along the northern edges of both the presented scenes (Figure 5b) after wave-bias correction and is likely related to underestimated wind-wave bias. In this context, the surface current retrievals at large incidence angles are likely more reliable than the ones at lower incidence angles. Moreover, in the western part of the Sentinel-1A scene (Figure 5b), the positive RVL values are assumed to be related to incorrect wind-wave bias correction resulting from inaccurate wind forecast. In the first swath in the Sentinel-1B scene (Figure 5a), the RVLs in general display notably larger values compared to the other swaths. It is likely due to uncertainties in the range Doppler bias calibration and may be connected with insufficient information in the ascending pass acquisition over land (Figure 5a).

3.2. Evaluation Against HFR Observations

The Sentinel-1 SAR-based RVLs were projected to the CODAR SeaSonde grid with a spatial resolution of about 5 × 5 km. To reduce the amount of noisy SAR data, pixels with Doppler shift standard deviation more than 3 Hz (about 0.15 m/s) were discarded. Moreover, all HFR pixels with spatial-temporal error >0.25 m/s were also discarded. Taking into account the spatial resolution of the HFR grid, we also discarded all pixels located closer than 10 km (i.e., 2 pixels) from the coast. This is necessary in order to exclude possible land interference in the Doppler acquisitions and also to avoid strong influence of the coastal topography on the near-surface wind field. Although this reduces the data set (by 42%), there is still a sufficient amount of data (279 samples) for the evaluation. The RVL retrievals from both ascending and descending passes were compared to the HFR-based RVL retrievals along four different beams, parallel to the SAR range directions (see Figure 6). Due to the satellite orbit configuration, HFR beams number 1 and 3 were collocated with scenes acquired in descending pass, while beam number 2 and 4 were collocated with scenes acquired in ascending pass. The differences between the SAR range and HFR beam directions were within ±2.5°. Furthermore, scenes for which only 1–2 pixels (per scene) were collocated were excluded from the analysis. This left us with 15 SAR scenes available for evaluation against the HFR measurements.

The scenes were acquired in a wide range of wind regimes, as indicated in Table 1 with wind speed ranging from 4 to 14 m/s (e.g., onshore and offshore wind directions, and azimuth/range parallel wind). The sea state at each collocated pixel was obtained from the wave model, yielding conditions for deep water waves. In general, the wave propagation direction is in agreement with the observed wind directions, with significant wave height and wave length, respectively, ranging from 0.1 to 3.5 m and 6 to 160 m.

The mean biases and RMSDs between the collocated measurements are also summarized in Table 1. The RMSDs range from 0.20 to 0.29 m/s, whereas the mean biases are between −0.12 and 0.12 m/s. As stated in the ESA Data User Element (DUE) GlobCurrent User Requirement Document (Donlon, 2013), the accuracy of surface current measurements at 30 km resolution should be within 5–30 cm/s depending on the application. The RMSDs between SAR and HFR retrievals are in the upper range of this interval. This suggests that

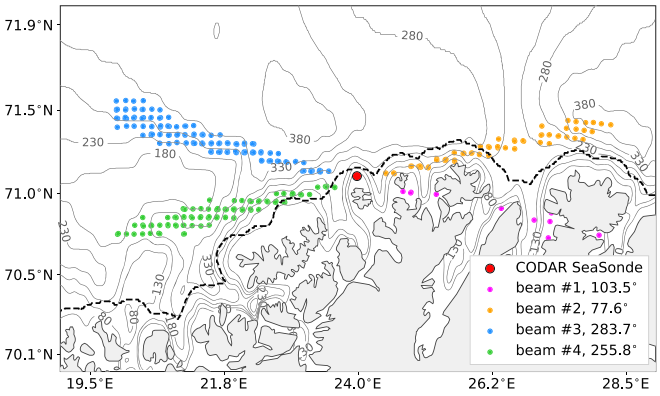

Figure 6. Positions of all collocated SAR and HFR acquisitions. The color code is labeled in the lower right. Black dashed line denotes 10 km margin to the nearest coastline. Gray lines are bathymetric contours.

the Sentinel-1 IW mode observations may indeed provide new and valuable estimates of the ocean surface current in the radial direction (for different wind and sea state conditions).

Comparison of the RVL retrievals (see section 3.1) to the HFR observations demonstrates a good agreement (Figures 7a and 7b) in terms of the mean biases (0.12 and 0.10 m/s) and RMSDs (0.20 and 0.24 m/s). The scenes were acquired during strong onshore wind (Sentinel-1B) and variable wind field (Sentinel-1A) with wind speed >12 m/s and significant wind wave heights of 2–3.5 m. In general, winds >7 m/s is considered to be the threshold for breaking waves.

The Sentinel-1A (Figure 7a) scene reveals a good correlation with the HFR ($r \approx 0.72$). On the other hand, the lower correlation ($r \approx 0.41$) in the Sentinel-1B scene (Figure 7b) is partly explained by three distinct outliers (14% of all collocated pixels) observed in the data set with 12 times larger mean bias (0.51 m/s) compared with the other 24 collocated pixels at a mean bias of 0.04 m/s. These outliers may be related to breaking wave events, which is expected to randomly occur at different locations in a particular moment of time. Breaking waves are not included in the wave model simulations. Hence, as the outliers are removed, we obtain a much better correlation ($r \approx 0.61$).

For the remaining nine scenes, the RMSDs (0.4 to 0.9 m/s) and the mean biases (−0.73 to 0.59 m/s) were unsatisfactorily large. Two of the nine scenes, however, demonstrate good agreement with the HFR retrievals in parts of the scenes. For the Sentinel-1B scene shown in Figure 7c (19 October 2017), we can see that the collocated pixels are separated into two clusters related to before and after the wind-wave bias correction. Each cluster is associated with pixels from different SAR swaths. Observations acquired in the third swath (8 pixels) demonstrate much better performance (mean bias of 0.01 m/s and RMSD of 0.17 m/s) than observations in the second swath (mean bias of 0.53 m/s and RMSD of 0.55 m/s). This is most likely related to inaccurate residual range Doppler bias correction. We also observe that pixels close to the swath

Table 1
Collocated Sentinel-1 Scenes and HFR Observations From October 2017

Scene	Date/time	Platform	Pass	*N*	Wind speed (m/s)	Wind dir. (deg.)	Mean bias (m/s)	RMSD (m/s)
SC1-R	2017-10-21 05:02:50	S1B	Desc.	11	8.7	347	−0.12	0.22
SC2-R	2017-10-25 05:20:12	S1A	Desc.	7	7.1	211	−0.10	0.25
SC3-R	2017-10-25 15:50:50	S1B	Asc.	24	4.9	211	0.03	0.24
SC4-R	2017-10-27 05:03:26	S1A	Desc.	6	13.7	259	0.12	0.20
SC5-R	2017-10-30 15:58:51	S1B	Asc.	22	11.9	303	0.10	0.24
SC6-R	2017-10-31 15:51:46	S1A	Asc.	18	4.8	286	−0.07	0.29

Note. The wind direction is given with respect to the SAR antenna look direction, that is, 0/180° is upwind/downwind.

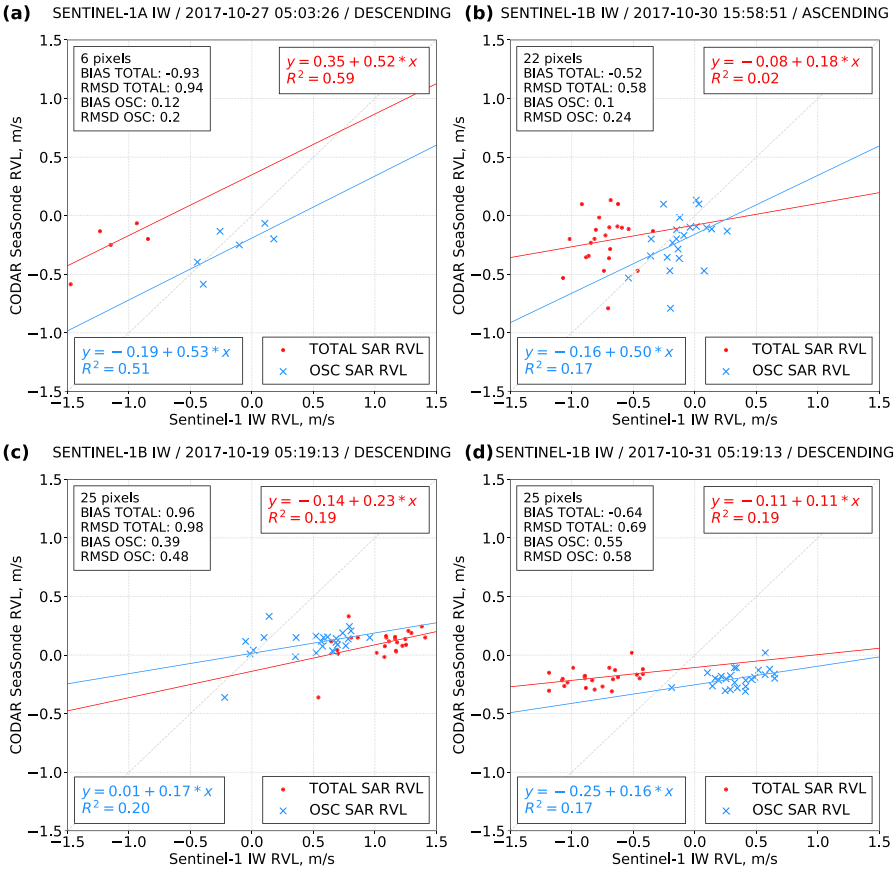

Figure 7. Comparison of the RVL retrievals from the CODAR SeaSonde HFR and the Sentinel-1 SAR observations for (a) 27 October, (b) 30 October, (c) 19 October, and (d) 31 October for the four scenes before (red dots) and after (blue crosses) wind-wave bias correction. The respective red/blue straight lines represent the linear regression between the observations.

edges frequently demonstrate larger differences with the HFR retrievals than pixels from other parts of the SAR images. Figure 3b also demonstrates discontinuities (jumps) in the Doppler shift observations acquired in different swaths. The larger errors observed for pixels close to the swath edges could indicate that the Doppler calibration algorithm is not always correct. As shown in Figure 3a, the Doppler shift could also vary strongly along azimuth. As detailed for Envisat ASAR by (Hansen et al., 2018), we speculate that part of this variation is caused by the Sentinel-1 satellite attitude variations. The use of Doppler shift observations over land for estimation and correction of biases over the ocean could in some cases be inaccurate, in particular for Sentinel-1, which has a less stable attitude than Envisat.

Comparison between the SAR- and HFR-based RVL retrievals before and after the wind-wave bias correction showed that for five of the analyzed scenes, incorrect wind forecasts most likely resulted in an erroneous wind-wave bias correction (i.e., Figure 7d). An indication of this is the significant increase of the RMSD (up to three times) after the wind-wave bias correction. In addition, geophysical factors such as breaking waves, intensive rainfalls, and small-scale wind features frequently observed in the SAR backscatter also affect the accuracy of the RVL retrievals. These factors, which create additional surface roughness not related

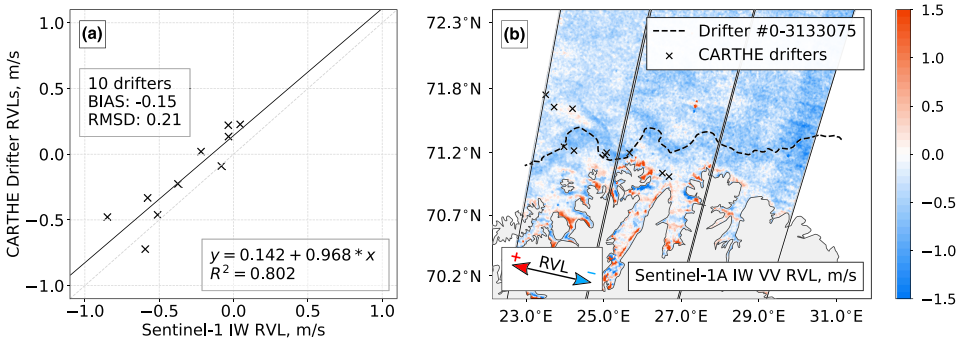

Figure 8. (a) Comparison of **OSC** RVL retrievals from Sentinel-1A scene acquired on 22 October 2017 04:54:59 with the collocated CARTHE drifter observations. (b) Sentinel-1A RVL scene with positions of the collocated drifters (x markers) and a drifter trajectory between 19 and 28 October 2017.

to the surface current, are ignored in the estimation procedure due to the relatively low spatial resolution (2.5 × 2.5 km) of the auxiliary NWP model simulations used to estimate the wind-wave bias.

3.3. Evaluation Against Surface Drifter Observations

A meandering pattern of the NCC is detected in most of the wind-wave bias corrected scenes. This is also confirmed by the CARTHE drifter trajectories, for example, from 19 October 2017 to 11 January 2018 and overlaid on the Sentinel-1A scene in Figure 8b.

The best agreement between the SAR and drifter retrievals is found at the southern rim of the Ingøy Trough, where the coastal current flow is stable due to strong topographical steering, which yields convergence of the drifter trajectories. In this region the NCC also flows nearly parallel to the SAR range direction, which is optimal for the SAR-based RVL detection. East of the Ingøy Trough, at the North Cape bank, the drifter trajectories are more chaotic (Figure 4) probably due to divergence of the NCC over the North Cape Bank (Skagseth et al., 2011).

The drifter velocity components aligned with the SAR radial directions were compared to the full resolution (pixel size 1.5 × 1.5 km) SAR-derived RVLs. By analogy to the HFR comparison, the SAR pixels of which the standard deviation of the Doppler shift was more than 3 Hz were discarded in the analysis. Since the size of the drifter data set is rather small and taking into account the finer resolution of the grid used in

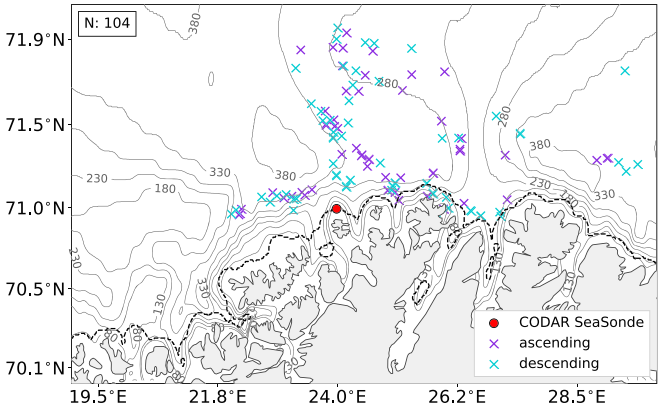

Figure 9. Positions of the ocean surface drifters collocated with the Sentinel-1 A/B acquisitions in ascending (purple markers) and descending (blue markers) passes. Black dashed line denotes 6 km margin to the nearest coastline.

Table 2
Sentinel-1 A/B Scenes from October 2017 Collocated With the CARTHE Ocean Surface Drifter Observations

Scene	Date/time	Platform	Pass	*N*	Wind speed (m/s)	Wind dir. (deg.)	Mean bias (m/s)	RMSD (m/s)
SC1-D	2017-10-19 05:19:13	S1B	Desc.	8	6.97	144	0.23	0.27
SC2-D	2017-10-19 15:51:46	S1A	Asc.	14	5.43	310	−0.11	0.30
SC3-D	2017-10-22 04:55:19	S1A	Desc.	10	5.67	142	0.15	0.25
SC4-D	2017-10-22 15:26:16	S1B	Asc.	6	4.07	71	−0.36	0.40
SC5-D	2017-10-25 15:50:50	S1B	Asc.	5	6.54	159	−0.12	0.21
SC6-D	2017-10-27 15:34:28	S1B	Asc.	6	11.2	177	−0.10	0.17

Note. The wind direction is given with respect to the SAR antenna look direction i.e., 0/180° is upwind/downwind.

this comparison, we reduced the distance to the nearest coastline from 10 to 6 km. Applying all the filter criteria yielded a reduction of 20% from the total of 104 collocated data points (Figure 9) derived from the 15 independent SAR scenes. We also required that a SAR scene should cover at least 5 drifters (i.e., 5 collocated pixels per scene). Despite this is not sufficient for reliable validation, it provides a valuable impression of SAR data quality. Therefore, only six scenes were available for analysis. The results of comparison are summarized in Table 2.

For almost all cases (five out of six) we observe good agreement between SAR-based RVL and the ocean surface drifter velocities with mean bias estimates from −0.12 to 0.23 m/s and RMSDs ranging from 0.17 to 0.30 m/s. The scenes cover a range of wind speeds from 4 to 12 m/s and significant wind wave heights from 1.5 to 3 m. All collocated samples were also acquired in the deep water conditions. We also found that for the scene demonstrated highest mean bias and RMSDs (Table 2, SC4-D), the range Doppler bias correction failed (not shown).

The scatter plot of the drifter radial velocities and SAR RVL from Sentinel-1A on 22 October 2017 (Table 2, SC3-D) (Figure 8a) shows good correlation ($r \approx 0.93$) with all 10 drifters detected within the scene (within second and third swaths). The mean bias is −0.16 m/s and the RMSD is 0.20 m/s. The first swath seems to demonstrate higher biases especially (at the lower incidence angles); however, it is not feasible to address it quantitatively due to lack of the collocated data. Similarly, the mean bias and RMSD estimates of RVL from the Sentinel-1A scene on 25 October 2017 (vs. HFR (Table 1, SC4-R) and surface drifters (Table 2, SC6-D)) did not exceed 0.25 m/s. In general, the agreement of the Sentinel-1 scenes to both the HFR and drifter observations are therefore promising.

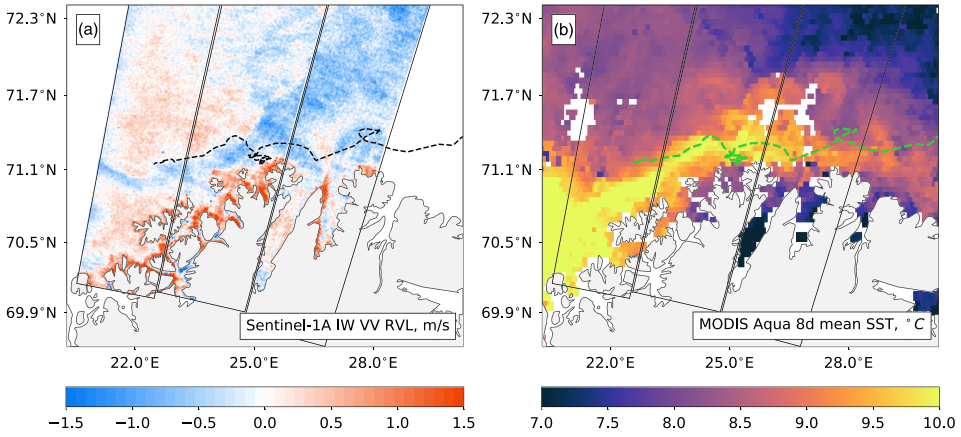

Figure 10. (a) Sentinel-1A IW RVL on 27 October 2017 05:03:26. (b) Average SST from MODIS Aqua observations (8 days, 8–16 October 2017). Black frames define SAR swath boundaries. The dashed lines indicate the trajectory of a surface drifter between 19 and 28 October 2017.

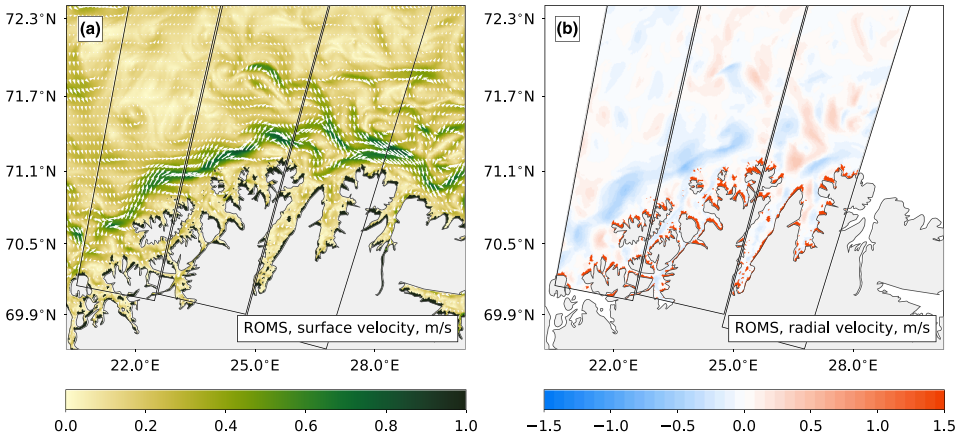

Figure 11. (a) Daily averaged simulated ocean surface velocity at 0 m depth from the ROMS model (MET Norway) from 27 October 2017. (b) Radial component of the ocean surface current derived by projecting the simulated velocity in the range direction of the corresponding Sentinel-1A scene from 27 October 2017 05:03:26.

3.4. Comparison to SST Field

The MODIS-Aqua SST field shown in Figure 10b (8-day average between 8 and 16 October 2017) displays a meandering SST frontal boundary with a mean east-northeastward orientation that compares well with the structure and orientation in the SAR-derived RVL on 27 October (Figure 10a). Moreover, the trajectory of the surface drifter (between 19 and 28 October 2017) shown in Figure 10b is largely confined to the core of the NCC as indicated by the SST field.

3.5. Comparison to the Ocean Model

The daily average ocean surface velocity field from the ROMS model interpolated at 0 m on 27 October 2017 is presented in Figure 11a. The NCC pattern observed in the model field generally shows good agreement with the SAR-based RVL field as shown in Figure 5a. The RVL field from the model (Figure 11b) was derived by projecting the simulated velocity in the range direction of the corresponding Sentinel-1 scene. The ROMS simulated currents are generally consistent with the SAR RVL retrievals. However, several inconsistencies are noted, especially in the western part of the domain. The RVL field derived from the model simulation shows that the flows northeast strongly along the coast in the southwestern part of domain (between 70.4°N and 70.9°N). This is not encountered in the SAR RVL field most likely due to incorrect wind-wave bias correction in the third SAR swath (see section 3.1). Second, the northern branch of the NCC that flows southeast at about 71°N and 22°E (see section 3.1) in the western part the SAR scene is not reproduced in the model simulations. We also note that the magnitude of the model RVL is generally lower than the satellite derived retrievals. The ocean surface circulation at the region is generally driven by two factors: wind regime and bottom topography. Hence, incorrect interpretation of any of those factors may yield underestimation of the current in the particular region. The ROMS is a free run model (i.e., no data assimilation). Therefore, despite observed disagreements, we conclude that generally, the model provides realistic high-resolution ocean surface currents (for the investigated cases).

The daily average ocean surface velocity field from the ROMS model interpolated at 0 m on 27 October 2017 is presented in Figure 11a. The NCC pattern observed in the model field generally shows good agreement with the SAR-based RVL field as shown in Figure 5a. The RVL field from the model (Figure 11b) was derived by projecting the simulated velocity in the range direction of the corresponding Sentinel-1 scene. The ROMS simulated currents are generally consistent with the SAR RVL retrievals. However, several inconsistencies are noted, especially in the western part of the domain. First, we see that according to the model the coastal current mostly flows strongly to the northeast along the coast in the southwestern part of domain. This is not encountered in the SAR RVL field most likely due to incorrect wind-wave bias correction in the third SAR swath. Second, the northern branch of the NCC that flows southeast at about 71°N and 22°E (see section 3.1) in the western part the SAR scene is not reproduced in the model simulations. We also note that the

magnitude of the model RVL is generally lower than the satellite derived retrievals. The ocean surface circulation at the region is generally driven by two factors: wind regime and bottom topography. Hence, incorrect interpretation of any of those factors may yield underestimation of the current in the particular region. The ROMS is a free run model (i.e., no data assimilation). Therefore, despite observed disagreements, we conclude that generally the model provides realistic high-resolution ocean surface currents (for the investigated cases).

4. Discussion

In this study, a number of Sentinel-1 A/B SAR IW RVL retrievals have been compared to coastal HFR and Lagrangian surface drifter data, as well as to satellite-based SST fields and modeled ocean surface currents. Under satisfactory calibration and wind-wave bias correction, the results demonstrate reliable estimates of the RVL derived from the Sentinel-1 SAR IW Doppler shift. The RMSD between SAR and HFR values are comparable or smaller than those presented in an earlier study for the Iroise Sea (Danilo et al., 2007). This is promising for future applications of Sentinel-1 SAR-based surface current retrievals. However, for some comparisons we also observe distinct disagreement. Both geophysical and nongeophysical factors contribute to this misfit.

The geometric (nongeophysical) Doppler frequency shift estimated from the satellite attitude and orbit control does not provide an accurate prediction of the actual geometric Doppler shift (Johnsen et al., 2016), as found in both azimuth and range directions. In addition, electronic mispointing provided by the antenna model also invoke inaccurate Doppler shift values. Previously, it has been demonstrated for Envisat ASAR wide swath (Hansen et al., 2011) and later for Sentinel-1 IW data (Johnsen et al., 2016) that images with land cover are preferable to derive reliable corrections of the biases caused by inaccurate geometry and electronic antenna mispointing. However, the uncalibrated data indicate that the satellite attitude, and thus the SAR pointing, can also change quite rapidly. Figure 3a, for instance, displays a periodic variation (scalloping) of the Doppler shift in the azimuthal direction. This is assumed to be a residual of the elevation directional antenna element pattern (AEP) envelope Kræmer et al. (2018) after the correction implemented in the Level 2 processor. The amplitude of this variation varies from swath to swath, and the pattern is most evident in the first image swath.

In general, the wind-waves contribution to the Doppler shift is calculated by invoking a forecast wind field from a numerical model to CDOP. In this study, the regional AROME-Arctic NWP model was selected due to its high spatial (2.5×2.5 km) and temporal (hourly) resolution covering the study region. While the near surface wind components from this model is in good agreement with in situ observations (see section 2.5), short-scale temporal-spatial variations of the wind field could be overlooked in comparison to the direct in situ point measurements. This may affect the ability to precisely estimate the wind-wave bias correction for the entire SAR scene. This effect is the most noticeable in case of the azimuth wind direction. The sign of the acquired Doppler shift is related to the relative moving of the ocean surface with respect to antenna look direction. As such, the upwind (toward the antenna) and downwind (away from the antenna) cases will demonstrate biases of opposite signs. Hence, the changing of the wind direction from upwind to downwind (due to inaccurate model prediction) yields a change of sign in the bias estimation.

Moreover, the CDOP is based on a fully developed (fetch unlimited) wind-sea assumption, meaning that the wind force a surface drift of 3% of the wind speed at 10 m height in each collocation (ECMWF and SAR) point. In the deep water case (i.e., topography does not influence the surface waves), the wind wave height is a function of the wind speed, fetch, and time in terms of persistency of the wind field. Thus, this assumption provides a big constraint for the analysis, especially in the coastal zone, where fetch limited seas are likely to occur for offshore wind fields.

The information about the near-surface wind speed and significant wind wave height acquired from the collocated atmosphere and wave models was used in order to check whether the fully developed sea assumption holds in the collocated SAR and HFR points (Figure 12). For simplicity, we divided all samples into three wind regimes: offshore, onshore, and alongshore. Evidently, the wave height is systematically lower than the idealized wave height expected for fully developed sea. This applies for all the three wind fields (speed and direction). As expected, the significant wave height is in agreement with near surface wing speed in both both onshore and offshore cases (with $r \approx 0.87$ and $r \approx 0.95$ correspondingly). Moreover, the difference in wave height for offshore and onshore conditions is minor for winds below 7 m/s. The fetch for fully

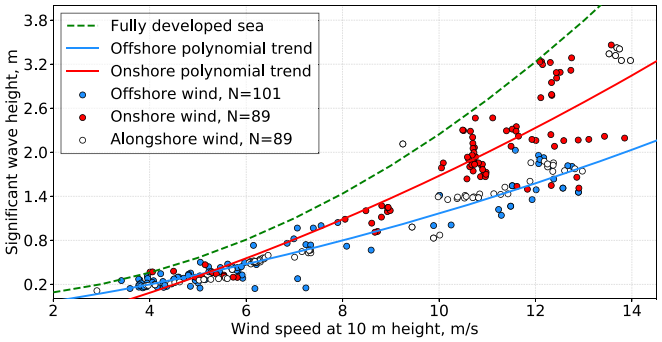

Figure 12. Comparison of the significant wind wave height from the MyWAVE model (MET Norway) with the near surface wind speed from AROME-Arctic model for the offshore (blue), onshore (red) and alongshore (white) winds. The dashed green line represents a theoretical relation for the fully developed sea.

developed seas in this case is typically below 50–60 km over time scale of few hours. For stronger winds, however, the difference rapidly increases. For the onshore winds (i.e., no fetch limitation) the significant wave height is closer to the theoretical goal, and in the absence of fetch limitation, its variation is likely to be related to the temporal instability of the wind field. In contrast, for the offshore, fetch limited cases, the wave height is about two times lower than the theoretical values. Note that for offshore winds of 10–15 m/s the fully developed seas would be encountered at approximately 100–500 km offshore. These distances are not compliant with our study in the near-shore region. Hence, we observe much less variation in the wave height with respect to the main tendency in offshore cases (RMSD is 0.16 m) compare with onshore cases (RMSD is 0.4 m).

All in all, the evaluation of the SAR scenes acquired under the different wind regimes did not provide any clear evidence on the performance of the method. This is partly related to the fact that the Sentinel-1 SAR azimuth direction in the study area (~350° and ~190° for ascending and descending passes) are respectively aligned with the typical offshore and onshore wind directions. As such, waves propagating in the near azimuth direction do not have a strong impact on the Doppler shift acquisitions that is predominantly encountered in the range direction. Moreover, whether or not the assumption about fully developed seas holds on the global scale, these signals should also be accounted for in the wind-wave bias correction model, for example, by considering the wind history and the wave spectrum at each collocation point.

All instruments and their observation characteristics utilized in this study provide estimates of the ocean current at different depths, for example, respectively <0.01, ~0.6, and ~2.5 m for the Sentinel-1 SAR, CARTHE drifters, and the HFR. These depths will certainly be exposed to different impact from the forcing field (e.g., wind and heat flux). In turn, the current speed will both have diurnal cycle and seasonal changes due to the upper layer stratification. The incoming solar radiation, freshwater runoff, precipitation, and mixing due to the near-surface wind and waves are all influencing this mixed layer variability and thus vertical shear of the ocean current. In addition, the wave-induced Stokes drift exponentially decreases with the depth. The surface currents derived from HFR are typically interpreted as Eulerian surface currents (e.g., Röhrs et al., 2015), which is related to the vertical integration of observed signal (over the first 2.5 m in our case). Hence, the HFR RVL include limited wave-induced Stokes drift. The SAR, on the other hand, measures the total signal from the moving ocean surface including the Stokes component. In turn, the Stokes drift could explain a fraction of the difference between HFR and SAR observations.

The quality of the reference observations must also be considered. The HFR observations have a rather large uncertainty (up to 0.25 m/s after filtering). Taking into account the required accuracy in the OSC retrievals, these data cannot be properly used as a reliable ground truth reference for validation of the SAR-based RVL retrievals. In comparison, the ocean surface drifter observations have an uncertainty of about 0.06 m/s. Thus, the comparison to the surface drifters is more reliable for the assessment of the quality of the SAR RVL retrievals, despite the small amount of collocated drifters (per scene).

The general structure of the surface current observed from the SAR is in good agreement with the respective ROMS model simulations. Nevertheless, some dynamical features were expectably not reproduced by the free run (i.e., no data assimilation) model simulations. Sperrevik et al. (2015) demonstrated that assimilation of the RVL derived from the coastal HFR improves the model simulations (positioning of eddies and current speed). The operational Sentinel-1 A/B SAR platforms could therefore provide high spatial resolution RVL maps up to two times per day (for high-latitude regions). In light of the given spatial-temporal characteristics and accurate calibration, the SAR-based RVL retrievals could therefore provide valuable information for validation and assimilation in numerical ocean models.

5. Conclusions

In this study, Sentinel-1 A/B IW mode SAR Doppler frequency shift observations have been used to retrieve surface velocity estimates of the NCC along the northern coast of Norway, with a spatial resolution of about 1.5 by 1.5 km. The intercomparison and assessment of these products have been carried out through collocation with land-based HFR measurements and Lagrangian sea surface drifter observations. In addition, the RVL retrievals have been compared to the surface current field derived from the ROMS model.

The analysis of the Sentinel-1 SAR data shows that distinct patterns of the NCC can be detected with range directed currents reaching up to 0.7 m/s. The absolute mean bias between SAR and HFR observations was 0.1 m/s, and the Root Mean Square Deviation (RMSD) was 0.24 m/s. In comparison, the agreement between the SAR-derived current features and the trajectories from Lagrangian surface drifters showed a mean bias 0.14 m/s and an RMSD of 0.24 m/s. Taking into account the uncertainty in the HFR data sets, the comparison and assessment to the ocean surface drifters provide the most reliable estimate of the SAR RVL retrieval accuracy.

According to the GlobCurrent users survey, the required accuracy of the horizontal ocean surface current velocity is in the range of 0.1 to 0.3 m/s (depending on region and application). As such, the comparison demonstrate that the use of SAR for ocean surface current retrieval is promising.

However, retrieving reliable surface current estimates from single pixels is still a major challenge, in particular due to the calibration of the range and azimuthal bias in the SAR Doppler shift observations. The calibration of the Level 2 RVL products performed in this study provides evidence that it is feasible on a case by case basis.

The sea state contribution to the geophysical Doppler shift provides an additional complicating factor for accurate ocean surface current retrievals. Precise calibration of the wind-wave bias relies on a GMF that requires near-surface wind field information derived from a numerical model. Thus, the accuracy of the model wind (both speed and direction) is crucial for precise calibration. In addition, the wave height and wavelength must also be taken into account.

Despite the relatively small number of investigated cases, the results are promising. However, it does not allow us to make any statistically significant conclusions. Further studies are required to develop a more reliable method for estimation of the wind and sea state impact on the SAR Doppler shift

Comparison of the ocean surface current derived from SAR with the ocean model simulations demonstrated a generally good consistency. Despite the model does not assimilate any observations, it well retrieves main circulation features in the region. However, some information available from SAR is evidently not present in the model. As such, the RVL retrievals from the Sentinel-1 could not only be a valuable resource for the model validation but also be considered for the future assimilation in the model simulations.

Acknowledgments
This work is performed under NERSC - 251348/F50 and CIRFA 970422528 projects funded by the Norwegian Research Council. We would like to thank the Norwegian Meteorological Institute (MET Norway) for providing HFR (The Norwegian Meteorological Institute, 2016), and meteorological observations as well as AROME-Arctic (The Norwegian Meteorological Institute, 2015), Wave (The Norwegian Meteorological Institute, 2016), and ROMS (The Norwegian Meteorological Institute, 2012, updated daily, 2012) model simulations. All these data sets are openly distributed via the MET Norway Thredds server (https://thredds.met.no/, CC 4.0 BY license). The Sentinel-1 products are distributed free of charge via Copernicus Open Data Hub (the data distribution is regulated under European Union law). Since, not all Sentinel-1 IW products are processed by European Space Agency to the Level 2 due to limited processing capacities. In this work, we used Level 2 products processed from Level 0 by NORCE Norwegian Research Center AS (Troms, Norway). These Level 2 data were then recalibrated using methodology from Johnsen et al. (2016). The processing chain is described in the article. Recalibrated data that were used in the analysis are available from the PANGAEA repository (Johnsen & Larsen, 2020). The ocean surface drifters data were provided by the Centre for Integrated Remote Sensing and Forecasting for Arctic Operations (CIRFA, Troms, Norway). Information from the drifters is openly available from the Zenodo repository (The Norwegian Meteorological Institute, 2020).

References

Abascal, A. J., Sanchez, J., Chiri, H., Ferrer, M. I., Cárdenas, M., Gallego, A., et al. (2017). Operational oil spill trajectory modelling using HF radar currents: A northwest European continental shelf case study. *Marine Pollution Bulletin*, *119*(1), 336–350. https://doi.org/10.1016/j.marpolbul.2017.04.010

Albretsen, J. (2011). Norkyst-800 report no. 1: User manual and technical descriptions (Tech. Rep.). Pb. 1870 Nordnes, N-5817 Bergen, Norway: Institute of Marine Research.

Barrick, D. E., Evans, M., & Weber, B. (1977). Ocean surface currents mapped by radar. *Science*, *198*(4313), 138–144.

Bonjean, F., & Lagerloef, G. S. (2002). Diagnostic model and analysis of the surface currents in the tropical Pacific Ocean. *Journal of Physical Oceanography*, *32*(10), 2938–2954. https://doi.org/10.1175/1520-0485(2002)032<2938:DMAAOT>2.0.CO;2

Breivik, Ø., Allen, A. A., Maisondieu, C., & Olagnon, M. (2013). Advances in search and rescue at sea Topical Collection on Advances in Search and Rescue at Sea. *Ocean Dynamics*, *63*(1), 83–88. https://doi.org/10.1007/s10236-012-0581-1

Chapron, B., Collard, F., & Ardhuin, F. (2005). Direct measurements of ocean surface velocity from space: Interpretation and validation. *Journal of Geophysical Research*, *110*, C07008. https://doi.org/10.1029/2004JC002809

Copernicus (2017). Sentinel-1 data. Retrieved from scihub.copernicus.eu (Accessed: 2019-09-30).

Danielson, R. E., Johannessen, J. A., Quartly, G. D., Rio, M. H., Chapron, B., Collard, F., & Donlon, C. (2018). Exploitation of error correlation in a large analysis validation: GlobCurrent case study. *Remote Sensing of Environment*, *217*(July), 476–490. https://doi.org/10.1016/j.rse.2018.07.016

Danilo, C., Chapron, B., Mouche, A., Garello, R., & Collard, F. (2007). Comparisons between HF radar and SAR current measurements in the Iroise sea. In *Oceans 2007-Europe*, Aberdeen, UK, 2007 (pp. 1–5). https://doi.org/10.1109/OCEANSE.2007.4302424

Davis, R. E. (1985). Drifter observations of coastal surface currents during CODE: The statistical and dynamical views. *Journal of Geophysical Research*, *90*(C3), 4756–4772. https://doi.org/10.1029/JC090iC03p04756

Donlon, C. (2013). ESA Data User Element (DUE) GlobCurrent user requirement document (URD) (Tech. Rep.). The Netherland: European Space Research and Technology Centre, Keplerlaan 1, 2201, AZ Noordwijk.

Edwards, M. (1989). *Global gridded elevation and bathymetry on 5-minute geographic grid (ETOPO5)*. Boulder, Colorado, USA: NOAA, National Geophysical Data Center.

Ekman, V. W. (1905). On the influence of the Earth's rotation on ocean-currents. *Journal of Functional Analysis*, *8*(3), 450–468. https://doi.org/10.1016/0022-1236(71)90006-1

Engen, G., & Johnsen, H. (2010). Sentinel-1 doppler and ocean radial velocity (RVL) algorithm definition. P.O. Box 6434, N-9294 Tromsø: Northern Research Institute.

Engen, G., & Larsen, Y. (2011). Efficient full aperture processing of tops mode data using the moving band chirp *z*-transform. *IEEE Transactions on Geoscience and Remote Sensing*, *49*(10), 3688–3693. https://doi.org/10.1109/TGRS.2011.2145384

GlobCurrent Team (2015). Globcurrent analyses and interpretation framework. http://www.globcurrent.org

Hansen, M. W., Collard, F., Dagestad, K. F., Johannessen, J. A., Fabry, P., & Chapron, B. (2011). Retrieval of sea surface range velocities from envisat ASAR doppler centroid measurements. *IEEE Transactions on Geoscience and Remote Sensing*, *49*(10), 3582–3592. https://doi.org/10.1109/TGRS.2011.2153864

Hansen, M. W., Johannessen, J. A., & Raj, R. (2013). Mapping the Nordic Seas surface velocity using Envisat ASAR. In L. Ouwehand (Ed.), *SeaSAR 2012, Proceedings of the conference held 18-22 June 2012 at Tromsø, Norway* (pp. 117–127). ESTEC, Noordwijk, The Netherland: ESA Comunications.

Hansen, M. W., Johnsen, H., Park, J.-W., & Engen, G. (2018). A new look at Envisat ASAR range Doppler shift retrieval with the aim of reprocessing ten years of level-0 data, *Eusar 2018; 12th european conference on synthetic aperture radar* (pp. 1–6).

Hansen, M. W., Korosov, A., Park, J.-W., Moiseev, A., & Danielson, R. (2019). nansencenter/django-geo-spaas: Django-Geo-SPaaS-0.2. Zenodo. Retrieved from https://doi.org/10.5281/zenodo.3476023

Hansen, M. W., Kudryavtsev, V., Chapron, B., Johannessen, J. A., Collard, F., Dagestad, K. F., & Mouche, A. A. (2012). Simulation of radar backscatter and Doppler shifts of wave-current interaction in the presence of strong tidal current. *Remote Sensing of Environment*, *120*(February 2012), 113–122. https://doi.org/10.1016/j.rse.2011.10.033

Haza, A. C., D'Asaro, E., Chang, H., Chen, S., Curcic, M., Guigand, C., et al. (2018). Drogue-loss detection for surface drifters during the Lagrangian Submesoscale Experiment (LASER). *Journal of Atmospheric and Oceanic Technology*, *35*(4), 705–725. https://doi.org/10.1175/JTECH-D-17-0143.1

Johannessen, J. A., Chapron, B., Collard, F., Kudryavtsev, V., Mouche, A., Akimov, D., & Dagestad, K. F. (2008). Direct ocean surface velocity measurements from space: Improved quantitative interpretation of Envisat ASAR observations. *Geophysical Research Letters*, *35*, 1–6. https://doi.org/10.1029/2008GL035709

Johannessen, J. A., Raj, R. P., Nilsen, J. E. Ø., Pripp, T., Knudsen, P., Counillon, F., et al. (2014). Toward improved estimation of the dynamic topography and ocean circulation in the high latitude and Arctic Ocean: The importance of GOCE. *Surveys in Geophysics*, *35*(3), 661–679. https://doi.org/10.1007/s10712-013-9270-y

Johnsen, H., & Larsen, Y. (2020). Collection of Sentinel-1 OCN Level 2 RVL products from October and and November 2017 processed for the Fruholmen experiment. [data set]. PANGAEA https://doi.org/10.1594/PANGAEA.913243

Johnsen, H., Nilsen, V., Engen, G., Mouche, A. A., & Collard, F. (2016). Ocean Doppler anomaly and ocean surface current from Sentinel-1 TOPS mode, *2016 IEEE International Geoscience and Remote Sensing Symposium (IGARSS)* (pp. 3993–3996). https://doi.org/10.1109/IGARSS.2016.7730038

Korosov, A. A., Hansen, M. W., Dagestad, K.-f., Yamakawa, A., Vines, A., & Riechert, M. (2016). Nansat: A scientist-orientated Python package for geospatial data processing. *Journal of Open Research Software*, *4*, e29. https://doi.org/10.5334/jors.120

Korosov, A., Hansen, M. W., Yamakawa, A., Moiseev, A., Dagestad, K.-F., Vines, A., et al. (2019). nansencenter/nansat: Nansat-1.2.3. Zenodo Retrieved from https://doi.org/10.5281/zenodo.3476011

Kræmer, T., Johnsen, H., Brekke, C., & Engen, G. (2018). Comparing SAR-Based Short Time-Lag Cross Ice Drift Velocities. *IEEE Transactions on Geoscience and Remote Sensing*, *56*(4), 1898–1908. https://doi.org/10.1109/TGRS.2017.2769222

Lagerloef, G. S. E., Mitchum, G. T., Lukas, R. B., & Niiler, P. P. (1999). Tropical Pacific near-surface currents estimated from altimeter, wind, and drifter data. *Journal of Geophysical Research*, *104*(C10), 23,313–23,326. https://doi.org/10.1029/1999JC900197

Le Traon, P.-Y., Antoine, D., Bentamy, A., Bonekamp, H., Breivik, L. A., Chapron, B., et al. (2015). Use of satellite observations for operational oceanography: recent achievements and future prospects. *Journal of Operational Oceanography*, *8*(sup1), s12–s27. https://doi.org/10.1080/1755876X.2015.1022050

Lebedev, K. V., Yoshinari, H., Maximenko, N. A., & Hacker, P. W. (2007). Yomaha07: Velocity data assessed from trajectories of argo floats at parking level and at the sea surface. *IPRC Technical Note*, *4*(2), 1–16.

Lumpkin, R., & Flamant, P. (2013). Extent and energetics of the Hawaiian Lee Countercurrent. *Oceanography*, *26*(1), 58–65. https://doi.org/10.5670/oceanog.2013.05

Lumpkin, R., & Johnson, G. C. (2013). Global ocean surface velocities from drifters: Mean, variance, El Niño-Southern Oscillation response, and seasonal cycle. *Journal of Geophysical Research: Oceans*, *118*, 2992–3006. https://doi.org/10.1002/jgrc.20210

Müller, M., Batrak, Y., Kristiansen, J., Køltzow, M. A., Noer, G., & Korosov, A. (2017). Characteristics of a convective-scale weather forecasting system for the European Arctic. *Monthly Weather Review*, *145*(12), 4771–4787.

Maximenko, N., Lumpkin, R., & Centurioni, L. (2013). Ocean surface circulation. *International Geophysics*, *103*, 283–304. https://doi.org/10.1016/B978-0-12-391851-2.00012-X

Mouche, A. A., Collard, F., Chapron, B., Dagestad, K. F., Guitton, G., Johannessen, J. A., et al. (2012). On the use of doppler shift for sea surface wind retrieval from SAR. *IEEE Transactions on Geoscience and Remote Sensing*, *50*(7), 2901–2909. https://doi.org/10.1109/TGRS.2011.2174998

NASA Goddard Space Flight Center (2014). Sea-viewing Wide Field-of-view Sensor (SeaWiFS) Ocean Color Data. NASA Ocean Biology Distibuted Active Archive Center (OB.DAAC), Goddard Space Flight Center, Greenbelt MD. (Accessed: 2019-09-30) https://doi.org/10.5067/ORBVIEW-2/SEAWIFSOC.2014.0

Niiler, P. P., Maximenko, N. A., Panteleev, G. G., Yamagata, T., & Olson, D. B. (2003). Near-surface dynamical structure of the Kuroshio Extension. *Journal of Geophysical Research: Oceans*, *108*(C6), 3193. https://doi.org/10.1029/2002JC001461

Novelli, G., Guigand, C. M., Cousin, C., Ryan, E. H., Laxague, N. J. M, Dai, H., et al. (2017). A biodegradable surface drifter for ocean sampling on a massive scale. *Journal of Atmospheric and Oceanic Technology*, *34*(11), 2509–2532.

Röhrs, J., & Christensen, K. H. (2015). Drift in the uppermost part of the ocean. *Geophysical Research Letters*, *42*, 10,349–10,356. https://doi.org/10.1002/2015GL066733

Röhrs, J., Sperrevik, A. K., Christensen, K. H., Broström, G., & Breivik, Ø. (2015). Comparison of HF radar measurements with Eulerian and Lagrangian surface currents. *Ocean Dynamics*, *65*(5), 679–690. https://doi.org/10.1007/s10236-015-0828-8

Raj, R. P., Nilsen, J. E. Ø., Johannessen, J. A., Furevik, T., Andersen, O. B., & Bertino, L. (2018). Quantifying Atlantic Water transport to the Nordic Seas by remote sensing. *Remote Sensing of Environment*, *216*(May), 758–769. https://doi.org/10.1016/j.rse.2018.04.055

Rio, M.-H., Mulet, S., & Picot, N. (2014). Beyond GOCE for the ocean circulation estimate: Synergetic use of altimetry, gravimetry, and in situ data provides new insight into geostrophic and Ekman currents. *Geophysical Research Letters*, *41*, 8918–8925. https://doi.org/10.1002/2014GL061773

Rouault, M. J., Mouche, A., Collard, F., Johannessen, J., & Chapron, B. (2010). Mapping the Agulhas Current from space: An assessment of ASAR surface current velocities. *Journal of Geophysical Research*, *115*, C10026. https://doi.org/10.1029/2009JC006050

Rypina, I. I., Kirincich, A. R., Limeburner, R., & Udovydchenkov, I. A. (2014). Eulerian and Lagrangian correspondence of high-frequency radar and surface drifter data: Effects of radar resolution and flow components. *Journal of Atmospheric and Oceanic Technology*, *31*(4), 945–966. https://doi.org/10.1175/JTECH-D-13-00146.1

Sætre, R. (2007). *The Norwegian Coastal Current: Oceanography and climate*. Norway: Akademika Pub.

Shutler, J. D., Quartly, G. D., Donlon, C. J., Sathyendranath, S., Platt, T., Chapron, B., et al. (2015). *Progress in satellite remote sensing for studying physical processes at the ocean surface and its borders with the atmosphere and sea ice* (Vol. 40, pp. 215–246). https://doi.org/10.1177/0309133316638957

Skagseth, Ø., Drinkwater, K. F., & Terrile, E. (2011). Wind- and buoyancy-induced transport of the Norwegian Coastal Current in the barents sea. *Journal of Geophysical Research*, *116*, C08007. https://doi.org/10.1029/2011JC006996

Sperrevik, A. K., Christensen, K. H., & Röhrs, J. (2015). Constraining energetic slope currents through assimilation of high-frequency radar observations. *Ocean Science*, *11*(2), 237–249. https://doi.org/10.5194/os-11-237-2015

Stewart, R. H., & Joy, J. W. (1974). HF radio measurements of surface currents. In *Deep sea research and oceanographic abstracts* (Vol. 21, pp. 1039–1049). https://doi.org/10.1016/0011-7471(74)90066-7

Stokes, G. G. (1880). On the theory of oscillatory waves. Transactions of the Cambridge Philosophical Society. Cambridge University Press.

The Norwegian Meteorological Institute (2012). ROMS model results. MET Norway Thredds Service. Retrieved from https://thredds.met.no (Accessed: 2019-09-30).

The Norwegian Meteorological Institute (2015). AROME Arctic 2.5km (SURFEX). MET Norway Thredds Service. Retrieved from https://thredds.met.no (Accessed: 2019-09-30).

The Norwegian Meteorological Institute (2016). MyWaveWam 4km. MET Norway Thredds Service. Retrieved from https://thredds.met.no (Accessed: 2019-09-30).

The Norwegian Meteorological Institute (2016). Near-Real Time Surface Ocean Radial Velocity. MET Norway Thredds Service. Retrieved from https://thredds.met.no (Accessed: 2019-09-30).

The Norwegian Meteorological Institute (2020). CARTHE drifter trajectories acquired at Fruholmen domain in October 2017 to January 2018. Zenodo. Retrieved from https://zenodo.org/record/3703441. http://doi.org/10.5281/zenodo.3703441

Vincent, P., Johnsen, H., & Piantanida, R. (2018). Sentinel-1 product specification. S1-RS-MDA-52-7441: Collecte Localisation Satellites (CLS). Retrieved from https://sentinel.esa.int/web/sentinel/user-guides/document-library

Yurovsky, Y. Y., Kudryavtsev, V. N., Grodsky, S. A., & Chapron, B. (2019). Sea surface Ka-band Doppler measurements: Analysis and model development. *Remote Sensing*, *11*(7), 839.

JGR Oceans

RESEARCH ARTICLE
10.1029/2020JC016288

Special Section:
Remote sensing of ocean surface currents using Doppler techniques from planes and satellites

On Removal of Sea State Contribution to Sentinel-1 Doppler Shift for Retrieving Reliable Ocean Surface Current

A. Moiseev[1], H. Johnsen[2], J. A. Johannessen[1,3], F. Collard[4], and G. Guitton[4]

[1]Nansen Environmental and Remote Sensing Center, Bergen, Norway, [2]NORCE Norwegian Research Center AS, Tromsø, Norway, [3]Geophysical Institute, University of Bergen, Bergen, Norway, [4]OceanDataLab, Locmaria Plouzane, France

Key Points:
- Combining near-surface wind with sea state information into an empirical Doppler model improves accuracy of the wave-induced bias estimates
- The CDOP empirical geophysical model function (based on the Envisat ASAR observations) should not be reused for the Sentinel-1 observations
- The Doppler shift observations from Sentinel-1 can be used to study ocean surface currents globally at a monthly timescale

Correspondence to:
A. Moiseev,
artem.moiseev@nersc.no

Citation:
Moiseev, A., Johnsen, H., Johannessen, J. A., Collard, F., & Guitton, G. (2020). On removal of sea state contribution to Sentinel-1 Doppler shift for retrieving Reliable Ocean surface current. *Journal of Geophysical Research: Oceans*, *125*, e2020JC016288. https://doi.org/10.1029/2020JC016288

Received 20 MAY 2020
Accepted 21 AUG 2020
Accepted article online 26 AUG 2020

Abstract The Doppler frequency shift acquired by Synthetic Aperture Radar (SAR) contains information about ocean surface motion induced by waves and the underlying ocean currents in the radar range direction. An accurate estimate of the wave-induced contribution is therefore required to derive a reliable estimation of the ocean surface current. In this study, we developed an empirical model for estimating the wave-induced Doppler shift based on Sentinel-1B Wave Mode (WV) Level 2 Ocean products acquired from December 2017 to January 2018 collocated with wind field from ECMWF and wavefield from WAVEWATCH III. We found that the relationship between the wind field at 10 m height and the Doppler shift from Sentinel-1 is in agreement with previous findings based on ASAR observations. Retraining of the conventional CDOP model for the Sentinel-1 observations (CDOP-S) yields distinct improvements. We speculate that the improvement is due to different sensor properties and hence biases in the data. Moreover, combing wave and wind information into the model yield considerable improvements especially for the Southern Ocean and the North Pacific. Given accurate wave bias correction, the ocean surface radial velocity maps based on 2 months of Sentinel-1 acquisitions agree with ocean surface current climatology derived from multiyear drifter observations. This suggests that Sentinel-1 Doppler shift observations can be used to study ocean surface currents with 20 km spatial resolutions at a monthly time scale.

Plain Language Summary The Doppler shift registered by Synthetic Aperture Radar (SAR) contains information about ocean surface motion associated with ocean waves and underlying ocean currents. An accurate estimate of the wave-induced contribution is crucial for retrieving reliable estimation of the surface current. In this study, we use observations from the Sentinel-1 SAR satellite collocated with wind and wave information from numerical models in order to develop an empirical model for estimating wave-induced Doppler shift. Based on the collocated data set we found that the relationship between the wind field and observed Doppler shift is in agreement with the literature. Difference between range wind speed and range wave orbital velocity can partly explain observed spread in the relationship between wind and observed Doppler shift. (Johannessen et al., 2008, https://doi.org/10.1029/2008GL035709) Combining wind and wave information into the empirical model yields a considerable improvement of the wave contribution estimates (compare with conventional models based only on wind information). The SAR derived ocean surface current (using the developed model) is in agreement with current derived from the conventional ocean surface drifter observations. Therefore, given correct wave bias estimates, Sentinel-1 observations can be used to systematically study ocean surface currents at a monthly time scale.

1. Introduction

The Doppler frequency shift acquired over the ocean by microwave Synthetic Aperture Radar (SAR) contains information about near-surface wind (Collard et al., 2008; Mouche et al., 2012) and ocean surface current (Hansen et al., 2011; Johannessen et al., 2008; Moiseev et al., 2020; Romeiser & Thompson, 2000) in the radar line-of-sight (hereafter range) direction (Chapron et al., 2005). The Doppler frequency shift is detected due to the motion induced by short Bragg resonant waves and their modulation by longer waves as well as the underlying ocean surface currents. In addition, the shift is also depending on the SAR antenna configuration (Chapron et al., 2005). In order to derive a reliable estimate of the range directed ocean surface current, it is therefore highly important to accurately determine and remove the wave-induced contribution to the Doppler shift signal.

The wind-wave-induced contribution to the Doppler shift (so-called wind-wave bias) has been documented under a range of environmental conditions and radar configurations (i.e., frequencies, incidence angles, and polarizations) (Martin et al., 2016; Mouche et al., 2012; Yurovsky et al., 2019). Empirical geophysical model functions (GMFs) such as CDOP (Collard et al., 2008; Mouche et al., 2012) are typically used for estimating wind-wave bias for given wind field and radar configuration. However, CDOP relies only on the collocated wind field product derived from ECMWF at the time of acquisition and largely ignores wave-induced contribution.

Sentinel-1 is an operational constellation of two SAR missions (A and B) providing continuous all-weather, day-and-night imagery at C-band with improved (compare to Envisat) revisit time, geographical coverage, and rapid data dissemination to support operational marine monitoring and applications. Recently, a novel data calibration technique based on the gyroscope telemetry from the satellites (OceanDataLab, 2019) has demonstrated promising capabilities to quantify the satellite attitude and hence provide reliable estimates of the Doppler shift. Hence, the wave-induced contribution to the Doppler shift (as established for the Envisat ASAR observations; Collard et al., 2008; Mouche et al., 2012) can now be revisited taking into account both wind waves and swell.

In this study, we take advantage of this new calibrated Sentinel-1 Wave Mode (WV) data set to develop an empirical model for estimating the wave-induced Doppler shift and, in turn, derive improved estimates of the ocean surface current. Section 2 describes the data and preprocessing steps and highlights the novel calibration of the Sentinel-1 WV Doppler shift observations. Section 3 presents an analysis of the Doppler frequency shift as a function of the near-surface wind field and ocean surface waves, followed by the development of a GMF for estimating sea state bias and its evaluation using independent data. Conclusions are presented in section 4.

2. Data and Methods

The data used in this study (Table 1) are provided in the standard Sentinel-1 Level 2 Ocean (OCN) products openly distributed via the Copernicus (Copernicus, 2017-2018) or downloaded from open sources. The main difference between the former Envisat ASAR Wave Mode Level 2 product and the Sentinel-1 OCN product is higher bandwidth (74.5 MHz vs. 16 MHz) and the Radial Velocity (RVL) component providing estimates of the Doppler Centroid (DC) frequency and the corresponding radial velocity. However, the gyroscope telemetry data are only available upon request directly to the European Space Agency (ESA).

2.1. Sentinel-1 WV Doppler Frequency Shift

We used Sentinel-1B Wave Mode (WV) Level 2 OCN RVL products acquired globally from December 2017 to January 2018 ($N = 78{,}190$). The WV products are obtained along two swaths centered at incidence angles of $\theta = 23°$ (from 21.6° to 25.1°, WV1) and $\theta = 36°$ (from 34.8° to 38.0°, WV2). The acquisitions are repeated every 100 km (within a swath), each covering an area of 20 × 20 km with a 5 × 5 m pixel size. In order to achieve a better signal-to-noise ratio and simplify the analysis, the mean DC value over the entire image area is estimated together with the incidence angle and azimuth direction. The estimated DC (f_{dc}) can be partitioned into contributions from the antenna, orbit/attitude, and geophysics yielding the following expression:

$$f_{dc} = f_{bias}(\beta) + f_{att}(\beta, \Theta_{att}(t)) + \underbrace{(f_{osc} + f_{ss})}_{f_{rvl}} \tag{1}$$

where

1. f_{bias} is the low-frequency (period >> orbital period) signal (bias) related to antenna electronic mis-pointing and low-frequency attitude variation;
2. f_{att} is the high-frequency (period << orbital period) satellite attitude variation;
3. Θ_{att} denotes attitude roll, pitch and yaw deviations from the nominal steering at time t;
4. β is off-boresight angle;
5. f_{rvl} is geophysical signal related to the ocean surface radial velocity (RVL) due to the combined wave-induced motion (f_{ss}) and the underlying ocean surface current (f_{osc}).

Table 1
Data Sets Used in the Study

Data set	Source	Temporal resolution	Spatial resolution[a]	Parameter (unit)	Data provider
Ocean surface radial velocity	S-1B WV Level 2 OCN	12 days[b]	20 km	Doppler shift (Hz), Incidence (deg.), Platform heading (deg.)	ESA/Copernicus
S-1B attitude variation[c]	S-1B gyroscope	2 s	—	Row, pitch, and yaw angles (deg.)	ESA (ODL, Aresys)
Near-surface wind field	ECMWF	1 hr	0.125°	Wind speed (m/s), wind direction (deg.)	ECMWF
Sea State parameters	WWIII	3 hr	0.5°	Significant wave height (m), mean period (s), mean direction (deg.)	IFREMER
Ocean current climatology	Drifter-Derived Climatology	1 Mth.[d]	0.25°	u, v components (m/s)	NOAA
Distance to the nearest coast	GMT	—	0.01°	Distance (km)	NASA's OBPJ
Bathymetry	GEBCO	—	0.015°	Ocean depth (m)	IHO, IOC

[a]The specified spatial resolution is before resampling on the Sentinel-1 grid. [b]Orbit repetition time (revisit time can lower and differ depend on the region). [c]The data set is not openly available. [d]Mean value for each month is estimated for each month based on multiyear observations (see Laurindo et al., 2017).

The high-frequency satellite attitude variation (f_{att}) is estimated using the pitch ($\Delta\theta_p$) and yaw ($\Delta\theta_y$) deviation angles derived from the gyroscope telemetry (OceanDataLab, 2019) which was available for the period of the study. These deviations are, in turn, converted to the corresponding frequency shift (OceanDataLab, 2019):

$$f_{att} = \frac{2vf_c}{c}\left(-\Delta\theta_y \sin\beta + \Delta\theta_p \cos\beta\right) \tag{2}$$

where v is the satellite velocity, f_c is the SAR frequency, and c is the speed of light. Ideally, f_{dc} observations acquired over land may be used for calibration of the f_{dc} acquired over the ocean (Hansen et al., 2011; Johnsen et al., 2016) since f_{rvl} over land is 0 Hz. In turn, the f_{bias} over the land can be derived as

$$f_{bias} = f_{dc} - f_{att} \tag{3}$$

Based on the assumption that this bias correction is also valid for the ocean acquisitions the total contribution from all non-geophysical terms expressed in Equation 1 are then known, allowing the geophysical signal (f_{rvl}) related to the ocean surface radial velocity (RVL) to be estimated.

Analysis of observations acquired over the land (Table 2) indicates 3 times larger mean bias in the WV1 acquisitions compared to the WV2. This difference is related to the antenna pattern which provides non-uniform bias depending on the incidence angle (Collecte Localisation Satellites, 2019). We also found a difference between observations from satellite ascending and descending tracks. We speculate that this might be related to a change in the satellite steering (configuration of Star Trackers) in the ascending orbit.

Moreover, up to 4 Hz variations in the Doppler shift at a period of about 300 orbits are also encountered over land for both WV1 and WV2 acquisitions (Figure 1). This variation is likely a result of the slow attitude variation not captured by the gyroscope data.

The following algorithm was proposed for removal of the non-geophysical components from the Doppler shift observations:

1. Select observations with 100% land coverage;
2. Estimate the f_{bias} (see Equation 3);
3. Estimate and remove mean value separately for WV1 and WV2 in ascending and descending passes;
4. Estimate mean f_{bias} for each orbit;
5. Fit residuals with a polynomial as a function of time separately for the WV1 and WV2 (see Figure 1);
6. Use the fitted model to calibrate the f_{rvl}acquired over the ocean.

Table 2
Statistics for Sentinel-1B WV Doppler Shift Observations Acquired Over the Land Presented Separately for the WV1 and WV2 Observations From the Ascending and Descending Passes

	WV1 ($\theta = 23^{\circ}$)						WV2 ($\theta = 36^{\circ}$)					
Data set	Ascending			Descending			Ascending			Descending		
Parameter	Mean	Med.	Std.	Mean	Med.	Std.	Mean	Med.	Std.	Mean	Med.	Std.
Observed Doppler shift[a]	27.56	27.01	5.51	23.50	23.90	5.55	8.65	8.42	5.08	5.26	5.20	4.90
Attitude corrected Doppler shift[b]	27.17	26.44	3.71	24.31	23.97	4.17	8.54	8.12	3.49	6.06	5.92	3.76
Residual bias corrected Doppler shift	0.38	−0.11	2.99	0.03	0.18	2.52	0.18	−0.06	2.85	0.50	0.21	2.22

[a]Corresponds to Equation 1. [b]Corresponds to Equation 3.

By removing the f_{att} components from the data set the standard deviations are reduced by about 1.8/1.6 Hz and 1.4/1.1 Hz for the WV1/WV2 ascending and descending passes respectively (Table 2). Removing the low-frequency biases the variations are further reduced by 0.7/0.7 and 1.7/1.5 Hz for the WV1/WV2 ascending and descending passes. The mean bias in all cases does not exceed 0.5 Hz.

After removal of all non-geophysical components, the ground range ocean surface radial velocity (u_d) at the WV1 and WV2 acquisitions can then be derived as Johannessen et al. (2008):

$$U_d = -\frac{\pi \cdot f_{rvl}}{k_e \cdot \sin\theta} \tag{4}$$

where k_e is the electromagnetic wavenumber and θ is the incidence angle.

2.2. Near-Surface Wind Field and the Sea State

Collocated information about the near-surface wind field and the sea state derived from numerical models was used for the analysis of the f_{rvl}. Wind speed (u_{10}, m/s) and direction (ϕ, deg.) at 10 m height were acquired from the European Centre for Medium-Range Weather Forecasts (ECMWF) Numerical Weather Prediction (NWP) model. The model provides hourly wind forecasts on the 0.125° grid. The wind field from the model is routinely resampled to the Sentinel-1 image grid and delivered with standard product specification (Collecte Localisation Satellites, 2019).

The model wind directions were first transformed to a coordinate system whereby the directions are provided with respect to the SAR antenna look direction:

$$\alpha_m^{'} = \alpha_m + \alpha_{sar} + \frac{\pi}{2} \tag{5}$$

where α_{sar} is the satellite azimuth direction and α_m is the wind direction in degrees from true North (in

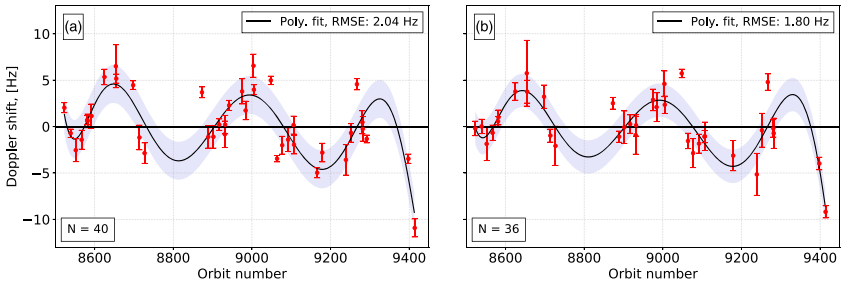

Figure 1. Orbit average Doppler frequency shift acquired over the land (red markers) acquired in (a) WV1 and (b) WV2 swath. The bars represent standard deviation of the Doppler shift within the orbit. Black line represents a polynomial fit for the observations and corresponding root mean squared error (RMSE).

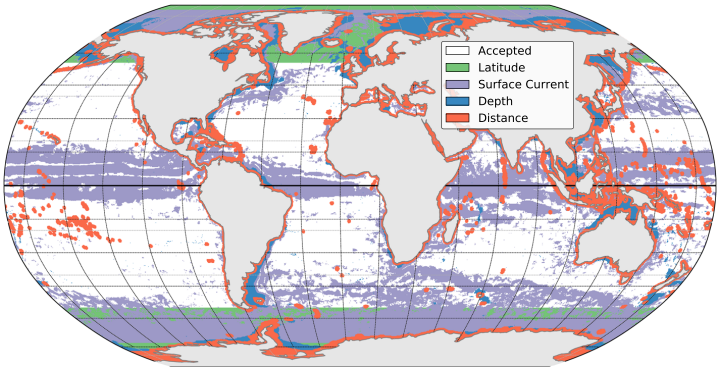

Figure 2. Global mask for selection of relevant Sentinel-B observations (white color) based on (green) latitude over 55; (purple) mean ocean surface current speed over 0.15 m/s (based on climatology from multiyear drifter observations); (blue) ocean depth below 1,000 m (based on GEBCO); (red) distance to the nearest coastline less than 110 km.

meteorological convention). After transformation, the 0° and 180° directions represent upwind (i.e., wind blows towards the radar) and downwind (i.e., wind blows away from the radar), while 90° and 270° represent azimuth winds (i.e., wind blows along the satellite track). The SAR range and azimuth vector components can be obtained as:

$$u_r = -u \cdot \cos\alpha_m^{'} \tag{6a}$$

$$u_a = -u \cdot \sin\alpha_m^{'} \tag{6b}$$

where u is wind speed.

Information about the sea state (combined wind waves and swell), at the position of the SAR acquisition, was extracted from the WAVEWATCH III model (Tolman, 2009). The model runs at the French Research Institute for Exploitation of the Sea (IFREMER) providing forecasts every 3 hr at a fixed 0.5° grid. The directional wave spectra are then resampled on the Sentinel-1 WV grid. However, the straight usage of the directional wave spectra is not practical, taking into account the large number of acquisitions. Moreover, it is also not practical in the view of building a new GMF, where only a limited number of input parameters can be considered. Therefore we simplified the analysis by deriving significant wave height (H_s, m), mean period (T_m, s), and mean propagation direction (ψ_m, deg.) from the total spectra (i.e., without partition for wind sea and swell) for each SAR image. As such we take into account the mean information about the ensemble of wave components at the time of the SAR acquisition. These parameters were used to estimate the wave orbital velocity:

$$\mathrm{u_w} = \omega_\mathrm{m} \mathrm{H_s} \tag{7}$$

where $\omega_m = 1/T_m$ is the mean wave frequency in Hz. Moreover, the wave propagation direction was transformed to the SAR antenna look direction (Equation 5) in consistence with the wind field transformation. Finally, the range and azimuth wave propagation directions were derived using Equations 6a and 6b.

2.3. Data Selection and Auxiliary Data Sets

Data-driven studies rely on the representativeness of the observations. In this regard, regions have been selected to limit observations affected by the surface current induced sea state variability, shallow water, coastal wind field variability, and presence of sea ice (Figure 2). Hence, the measured Doppler shifts are primarily considered to be resulting from motions induced by ocean surface waves. Regions, where the near-surface current speed was above 0.15 m/s, were determined from drifter climatology and removed from the analysis (yielding 37.7% of data). This approach limited unwanted biases invoked due to wave-current

Table 3
Summary of the Statistics of the Selected Wind and Wave Field Parameters for the WV1 and WV2 Collocations

Parameter	Notation	Units	Swath	Min	Mean, μ	Max	Std., σ
Incidence angle	θ	°	WV1	22.878	23.801	24.373	0.416
			WV2	35.932	36.819	37.366	0.415
Wind speed	u_{10}	m/s	WV1	0.145	7.642	23.415	3.299
			WV2	0.148	7.640	26.746	3.273
Wind direction	ϕ	°	WV1	0.007	174.537	359.988	105.473
			WV2	0.003	174.114	359.964	105.131
Significant wave height	H_s	m	WV1	0.332	2.646	10.712	1.097
			WV2	0.314	2.637	9.691	1.094
Mean wave period	T_m	s	WV1	3.518	7.594	14.085	1.290
			WV2	3.283	7.582	14.530	1.290
Mean wave direction	ψ_m	°	WV1	0.083	190.940	359.995	101.726
			WV2	0.013	189.106	359.999	100.595

Note. The wind and wave propagation directions are provided with respect to SAR antenna look direction.

interactions and the subsequent impact on the sea state (Ardhuin et al., 2017; Kudryavtsev et al., 2017). Moreover, as ocean bottom topography may also affect the surface wave field (Alpers & Hennings, 1984), regions shallower than 1,000 m (1.9% of the data set) were excluded. In addition, as the ECMWF wind field model does not properly account for orographic effects on the near-surface wind field, all pixels (5.3% of the data set) acquired closer than 110 km (i.e., about 2 model pixels) to the coast were also removed. Finally, in order to avoid the inference of sea ice, all observations acquired at latitudes above 55°N and 55°S (12.3% of the data set) were excluded. All in all, this selection constrain removed 43.9% of the initial data set leaving 43,857 Sentinel-1B WV collocated images available for the analyses (see Table 3) addressed in section 3.

3. Results

The analysis presented in this section is based on the 43,857 WV1 and WV2 Sentinel-1B SAR scenes subselected in section 2 and then collocated with the model-based wind- and wave fields, both transformed to the satellite native grid. In sections 3.1 and 3.2 the Doppler shifts ($f_{rvl} = f_{ss} + f_{osc}$) are examined in view of modifications induced by a wide range of near-surface wind field and sea state conditions (see Table 2) under the assumption of limited influence by the surface current. Building on this, section 3.3 presents a geophysical model function for estimating the sea state contribution to the Doppler shift. The retrievals of ocean surface currents are then presented in section 3.4.

3.1. Relationship Between the Doppler Shift and Near-Surface Wind Field

The relationship between the geophysical Doppler shift (f_{rvl}) and the near-surface wind speed (u_{10}) and direction (Chapron et al., 2005; Collard et al., 2008; Collecte Localisation Satellites, 2019; Mouche & Chapron, 2015) are shown in Figure 3. As expected, f_{rvl} increases with radial directed winds as well as increasing wind speed for both $\theta = 23^\circ$ and 36° as noticed in Figures 3a, 3b, 3d, and 3f. At $\theta = 23^\circ$ the f_{rvl} to u_{10} relationship increases as a cosine function of wind direction with respect to antenna direction (Equation 5) (Figure 3a). Maximum f_{rvl} corresponds to cases when the wind is strong and parallel to the antenna range direction. In contrast, the average $f_{rvl} \approx 0$ Hz when the wind blows along the satellite track (i.e., perpendicular to antenna range direction). The magnitude of the f_{rvl} is similar for upwind (i.e., when the wind blows toward antenna) and downwind (i.e., when the wind blows away from the antenna) cases, except for the highest wind speeds. In turn, the wave asymmetry which impacts the SAR signal (Collard et al., 2008; Mouche et al., 2012) is not detectable at $\theta = 23^\circ$ for winds below 10 m/s. The linear regression (Figure 3c) shows that the ocean surface radial velocity (Equation 4) derived from f_{rvl} is about 24% of the range wind speed (Equation 6a) which is consistent with findings reported by Chapron et al. (2004) and Chapron et al. (2005) based on Envisat ASAR observations.

In comparison $\theta = 23^\circ$, the observed f_{rvl} at $\theta = 36^\circ$ (Figures 3d and 3e) is generally smaller for winds above 5 m/s. The contribution from the slow-moving Bragg waves increases with increasing incidence angle

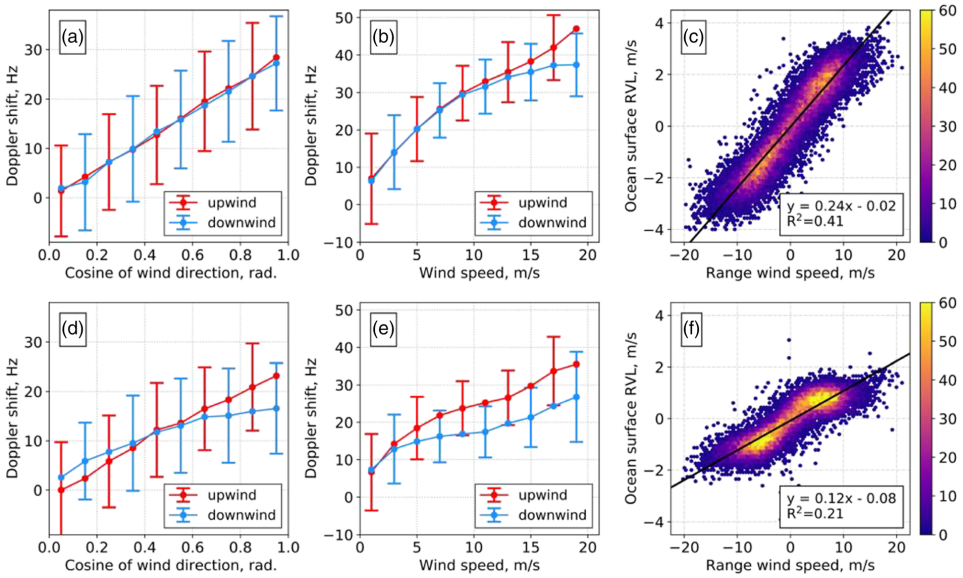

Figure 3. The geophysical Doppler shift f_{rvl} in VV polarization as a function of near surface radial wind direction (a, d) and wind speed (b, e) at WV1 (top row) and WV2 (bottom row). Vertical bars represent standard deviation of Doppler shift for the corresponding bin. Upwind (red)/downwind (blue) correspond to positive/negative shifts. The ocean surface radial velocity as function of radial wind speed are shown in (c, f). Color scale represent number of observations. The black line represents the linear regression (insert).

yielding a decrease in the f_{rvl} (Collard et al., 2008; Johannessen et al., 2008; Mouche et al., 2008). Moreover, as expected, the difference between upwind and downwind cases become recognizable at larger incidence angles. Both tilt and hydrodynamic modulations yield asymmetric distribution of the surface scatterers which, in turn, affects f_{rvl} depending on the wind and sea state conditions (Mouche et al., 2012; Yurovsky et al., 2019).

3.2. Relationship Between the Doppler Shift and Ocean Surface Wave Field

In order to study the combined effect of the wind and wave fields on the f_{rvl} the method proposed by (Yurovsky et al., 2019) has been applied. The relationship between wave orbital velocity (Equation 7) projected on SAR range direction (hereafter range wave velocity) and range wind speed for each available Sentinel-1B acquisition is shown in Figure 4. The biggest disagreement between wind and wave radial velocity is for low to moderate wind speeds (below 10–12 m/s). At low wind speed, the ocean surface wave field may be governed by the remotely generated swell. As the wind speed increases the local wind sea component starts to dominate yielding a better correlation between the range wind speed and wave orbital velocities. Temporal wind instability and fetch limitations will also contribute to the observed spread.

Following Yurovsky et al. (2019) the absolute distance from the observed range wave velocity to the linear trend (Figure 4a, color) was used as a measure of disagreement between wind and wave fields:

$$\Delta u_w = \left| u_w - u_w^{'} \right| \tag{8}$$

where $u_w^{'}$ is wave orbital velocity estimated from the linear regression (see Figure 4a, trend). Including Δu_w (Equation 8) in the analysis (Figures 4b and 4c, color) allows to describe a part of misfit between f_{rvl} and the range wind speed (Figures 4b and 4c, scatter), especially at low and moderate wind speeds. It also explains some outliers in the data set.

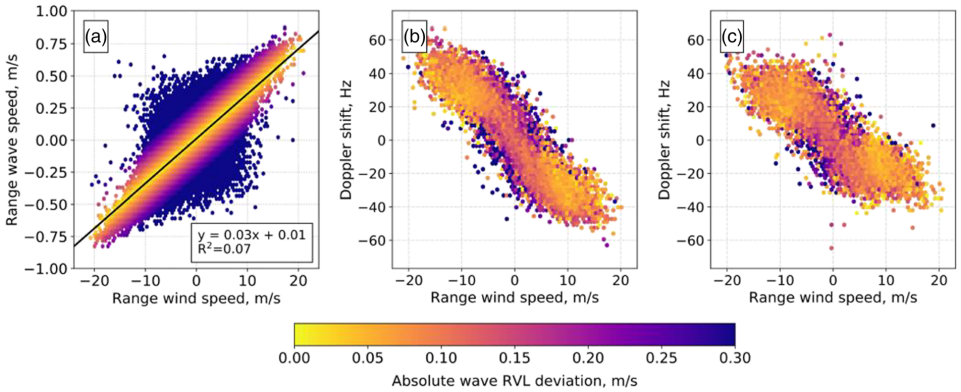

Figure 4. (a) Relationship between range directed wind velocity from ECMWF and range directed wave orbital velocity from the WAVEWATCHIII collocated to the Sentinel-1 SAR acquisitions. Black line represents linear regression. Color represent deviation of the range wave orbital velocity from the linear trend. Panels (b) and (c) represent Doppler frequency shift and range windspeed (scatter) and corresponding deviation of the range wave orbital velocity from the linear trend (contours) for the WV1 and WV2 correspondingly.

As the relationship between the Doppler shift and the near-surface wind is established (Figure 3), we moreover demonstrate that using only wind information is not sufficient (Figure 4) for assessing and estimating the wave contribution to the observed f_{rvl}. However, deriving an analytical formula for estimating wave-induced Doppler is still a challenge, taking into account the number of involved variables and their interactions. The artificial Neural Networks (NN) provide an opportunity to approximate any arbitrary complex function without any prior knowledge of the relationship between independent and dependent data. Hence we can take advantage of the amount of available observations to train a Geophysical Model Function designed to fit the Sentinel-1 WV data, taking into account more complete physical information about the sea state.

3.3. Sea State Bias Correction Model for the Sentinel-1 Doppler Shift Observations

Based on the C-band observations from Envisat ASAR, Mouche et al. (2012) developed an empirical geophysical model function (GMF) called CDOP for estimating the wind-wave-induced Doppler shift for a given wind field and SAR antenna configuration:

$$f_{ww} = CDOP(u_{10}, \phi, \theta, p) \tag{9}$$

where u_{10} is wind speed, ϕ is wind direction with respect to SAR antenna (Equation 4), θ is incidence angle, and p is polarization.

To establish a baseline for further model developments, the performance of the CDOP (Equation 9) for the Sentinel-1 acquisitions was investigated using 10% of randomly selected observations (hereafter test data). As shown in Figures 5a and 5d the CDOP predictions are generally in agreement with the observed f_{rvl}. However, the linear regression shows that CDOP systematically underestimates the f_{rvl} by 25–27%. Moreover, the model shows better results at WV2 compared with WV1, based on the estimated root mean squared error (RMSE) and linear regression bias. Taking into account the empirical nature of the CDOP model, the observed errors are considered to be explained by the fact that the model was trained on observations from a different satellite and hence inherits all corresponding biases in the data.

The CDOP model was therefore retrained (separately for the WV1 and WV2) to achieve a better fit with the Sentinel-1 WV observations (CDOP-S). First, all the independent variables (i.e., u_{10}, ϕ, θ) were normalized as $y = (x - \mu) \cdot \sigma^{-1}$ using the corresponding mean, μ, and standard deviation, σ, listed in Table 3. An open available Python TensorFlow library (Abadi et al., 2015) was then used to develop a three-layer Neural Network (NN) to fit the GMF. The main tradeoff using the NN, however, is that the examination of an internal

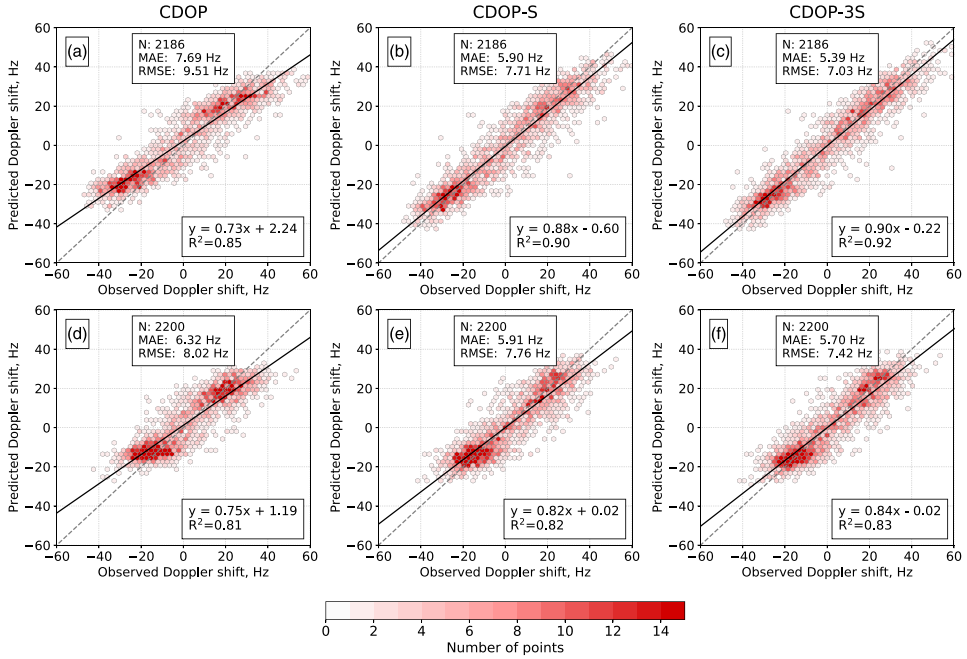

Figure 5. Comparison of the predicted Doppler shift to independent observations (scatter) for CDOP (a, d), CDOP-S (b, e), and CDOP-3S (c, f). Top and bottom rows represent cases for Sentinel-1B WV1 and WV2 correspondingly. Number of observations (*N*), mean absolute error (MAE), and root mean squared error (RMSE) for each model are indicated in the top center. Black line and inserted equation (right bottom corner) represent linear regression between observed and predicted Doppler frequency shift for each model.

structure of the network does not provide any insights on the impact of each independent parameter on the final estimate. Therefore at first instance, we evaluated and compared model performance based on the final fit acquired for preselected test data (not involved in training). Analysis based on this test data shows significant improvements of the CDOP-S performance compared to CDOP (Figures 5b and 5e), with particular improvement for the WV1 data where the RMSE decreased by 19% and LRS is increased to 0.89. In comparison, less improvements were encountered for WV2.

These promising findings are therefore used in the refined and new empirical model (CDOP-3S) for estimating the wave-induced contribution to the Sentinel-1 Doppler shift observations as expressed by:

$$f_{ss} = CDOP\text{–}3S(u_{10}, \phi, H_s, T_m, \psi_m, \theta, p) \tag{10}$$

The new variables in this expression include the significant wave height H_s, the mean total (i.e., combined wind waves and swell) wave period T_m, and the wave mean direction ψ_m with respect to the SAR antenna (Equation 4). The considerable improvement compared to CDOP-S are reached, especially for the WV1 data (Figures 5c and 5f). For the WV1 the RMSE decreased by 9% reaching 7 Hz and LRS is increased to 0.9. In contrast, for WV2 the RMSE decreased by 5% reaching 7.4 Hz while LRS is increased to 0.84.

3.4. Ocean Surface Radial Velocity Retrieval and Evaluation

The Doppler shift due to ocean surface current (f_{osc}) is obtained by subtracting the wave contribution ($\widehat{f_{ss}}$) from the observed geophysical Doppler shift:

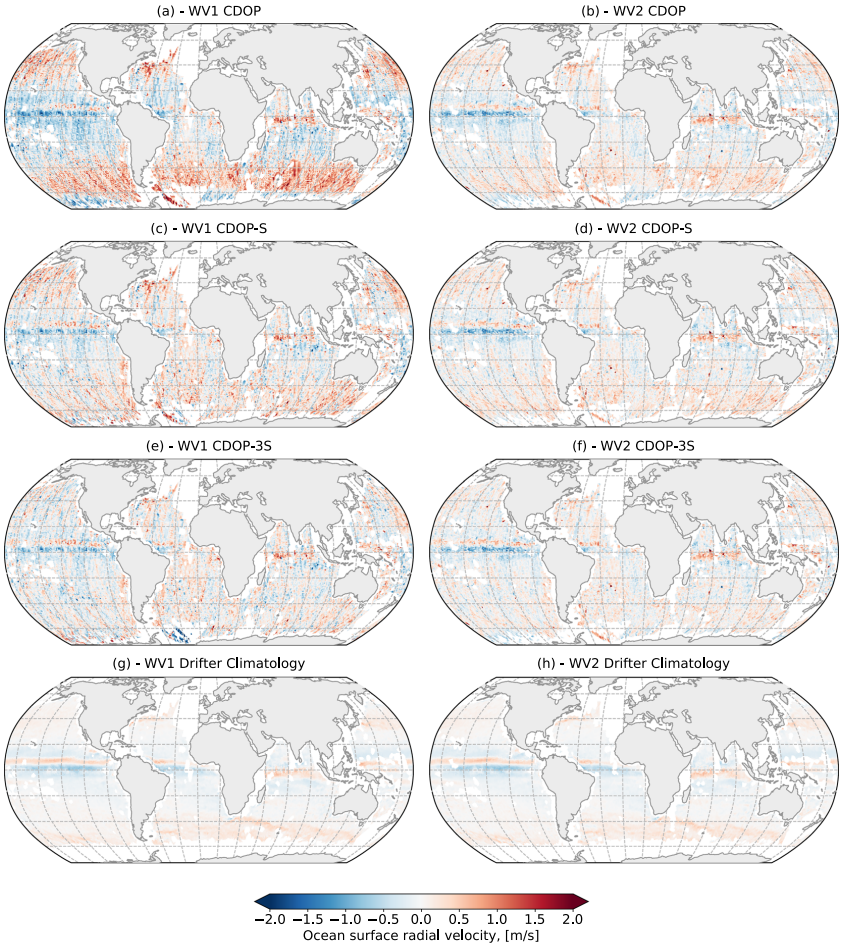

Figure 6. Gridded climatology of ocean surface current radial velocity (in m/s) based on 2 months of Sentinel-1B observations from combined ascending and descending passes. The SAR derived RVL was retrieved using CDOP (a, b), CDOP-S (c, d), and CDOP-3S (e, f) and compared to ocean surface drifter climatology (g, h). Positive (negative) values represent eastern (western flow).

$$f_{osc}^{m} = f_{rvl} - \widehat{f_{ss}^{m}} \tag{11}$$

where m represents the empirical model used for estimating wave contribution (i.e., CDOP, CDOP-S, or CDOP-3S). When these f_{osc} estimates are invoked into Equation 4, U_d, a gridded climatology of the U_d^{sar} can be derived using the 2 months of global Sentinel-1 SAR WV1 and WV2 observations. These SAR Doppler-based ocean surface current retrievals are then compared to the global near-surface ocean velocity climatology (U_d^{clim}) derived from the surface drifter observations (Laurindo et al., 2017) as shown in Figure 6. The Sentinel-1 WV observations, acquired every 200 km along the satellite orbit (see section 2.1) at both incidence angles while separated by 100 km in azimuth, were analyzed separately. In addition, the drifter climatology was first collocated and range projected to the corresponding SAR acquisition and then interpolated on the regular 0.2 × 0.2° grid in analogue with Doppler derived RVLs.

The equatorial current pattern is evident in the SAR derived ocean surface radial velocity maps independent on the choice of wave contribution model (Figures 6a–6f). The pattern, moreover, is in good agreement with the drifter climatology (Figures 6g and 6h). Analysis of the OSC maps derived using CDOP (Figures 6a and 6b) indicates strong residual signal related to the near-surface wind field, in particular in the Southern Ocean. This confirms that the CDOP underestimates wave contribution to the signal (see also Figures 5a and 5d). The residual signal is more pronounced in the WV1 data because of the stronger (up to 2 times, Figures 3c and 3f) sensitivity to the wind compare with the WV2.

Invoking the CDOP-S model yields noticeable improvement in the OSC retrievals (Figures 6c and 6d) compared to the CDOP. The global (between 55°N and 55°S) root mean square difference (RMSD) between U_d^{CDOP} and U_d^{CDOP-S} is about 0.30/0.11 m/s for the WV1/WV2) observations. However, the residual contribution from the wind field can still be observed especially in the midlatitudes (between 30° and 55°). This confirms that the CDOP cannot be routinely used for estimating the wind-wave contribution to the Sentinel-1 acquisitions. Taking into account the empirical nature of the models, we speculate that, since the physical assumptions are similar in both models, the observed deviations are due to differences in the two SAR sensors. This yields a corresponding impact on the geometric and electronic biases which are inherited in each model.

Including sea state information (i.e., CDOP-3S model) allows further reduction in the residual bias (Figures 6e and 6f), yielding RMSDs between U_d^{CDOP-S} and $U_d^{CDOP-3S}$ of about 0.22/0.11 m/s for the WV1/WV2. The best improvement, obtained in the midlatitudes, is about twice as good as for the equatorial region. This might be related to the frequency of severe storms occurring in the North Pacific, North Atlantic, and in the Southern Ocean which will create swell fields. In turn, by removing this wave contribution to the Doppler shift, expressions of the Gulf Stream and the Kuroshio Current can be manifested. However, the Sentinel-1 WV observations offer limited capacity for studying Western Boundary Currents (WBC) due to sparse coverage (these regions are usually covered by swath data). It is therefore it not possible to provide any sustainable conclusion about WBC, taking into account that only 2 months of observations were available for this study. Comparison of the $U_d^{CDOP-3S}$ with the U_d^{clim} showed that global RMSDs between two fields are 0.37/0.28 m/s for the WV1/WV2. These numbers indicate good agreement between the SAR derived OSC with traditional surface drifter climatology. Due to the finer spatial–temporal resolution of the SAR derived OSC more geophysical variability is expectedly contained in the Sentinel-1B data.

4. Discussion and Conclusions

In this study, a novel calibration technique based on gyroscope telemetry (OceanDataLab, 2019) has allowed us to investigate the quality of the radial ocean surface current retrievals derived from the Sentinel-1B Doppler shift observations. The Doppler shift contains information about ocean surface motion induced by waves and the underlying ocean currents in the radar range direction. An accurate estimate of the wave-induced contribution is therefore required to derive a reliable estimation of the ocean surface current. By incorporating model-based information of near-surface wind (ECMWF) and ocean waves (WAVEWATCHIII) into a Geophysical Model Function (GMF) we demonstrate that more accurate estimates of the wave-induced Doppler shift component can be derived. In turn, the retrieval accuracy of the ocean surface current is improved. Unfortunately, the gyroscope telemetry was only available in experimental mode from Sentinel-1B over 2 months from December 2017 to January 2018.

In order to examine the Doppler shift as a function of open ocean wind conditions and fully developed wave fields, the Sentinel-1B acquisitions were down-selected to avoid areas of strong surface currents, coastal areas with shallow water topography, and presence of sea ice. According to collocated ECMWF and WAVEWATCH III model simulations, we find that generally, the fully developed sea assumption remains valid as shown and commented in Figure 5a. It is found that the wind sea contribution to the Doppler signal is generally weaker at $? = 36°$ compared to $\theta \approx 23°$ for winds >5 m/s. Notably, the ocean surface radial velocity is about 12% (24%) of the range wind speed at $\theta \approx 36°$ ($\theta \approx 23)°$. However, while the contrasts between upwind and downwind results at $\theta \approx 23°$ are in good agreement with Yurovsky et al. (2019) (based on Ka-band Real Aperture Radar observations) they disagree with the findings reported by Mouche et al. (2012). This inconsistency may be explained by factors including differences in the SAR instruments used in each

study, in spatial resolutions and data calibration techniques. The wind field variability, fetch limitations, and presence of swell (especially at low wind speeds, when the ocean surface wave motion is governed by remotely generated waves) add additional spread in the observed dependency. Using WAVEWATCH III the difference between the wave orbital velocity in range direction and the range wind speed can potentially explain the observed spread, especially for the WV1 data (Figure 5b) where the sea state contribution is much larger compared to the WV2 data (Figure 5c).

By retraining the empirical CDOP model with Sentinel-1 WV observations (CDOP-S) the model accuracy clearly improves. This confirms the hypotheses that CDOP, due to its empirical nature, inherits biases from the Envisat ASAR observations, and as such, it cannot be directly reused for the Sentinel-1 observations. We also notice that CDOP performs better at higher incidence angle. Including wave information into the model (CDOP-3S) yields additional considerable improvements especially for the Southern Ocean and the North Pacific. This is explained by the frequent presence of storms in these basin regions that generate swell fields and crossing seas which, in turn, will affect the Doppler shift signals.

Ideally, retrievals of wave parameters from the Sentinel-1 WV Level 2 Ocean Surface Wave (OSW) product would yield an opportunity to move towards a GMF which solely relies on SAR data. Stopa et al. (2015) showed that the azimuth cut-off can provide valuable information about wave orbital velocity, based on collocated Envisat ASAR, WAVEWATCH III, and bouy data. However, the cut-off also provides a major constrain for dreiving reliable estimates of wave height, dominant wavelength, and direction from the OSW spectra. One way to overcome this may be to develop a robust partitioning of the wave spectra into wind waves and swell. Other wave field parameters such as mean squared slope and mean slope speed vector (Nouguier et al., 2018) have also been shown to provide characteristics of the wave-induced Doppler shift for the near-nadir observations and might be considered in the future work.

Given accurate wave bias correction and removal, the ocean surface radial velocity map from 2 months of Sentinel-1 acquisitions are found to be in good agreement with ocean surface current climatology based on surface drifter observations. As such, the Sentinel-1 B Doppler shift observations from the wave mode (WV1/WV2) acquisitions reveal promising capabilities for regular monitoring of equatorial ocean surface currents for 20 km resolution cells at a monthly time scale. Since the amount of wave mode acquisitions over the Western Boundary Currents (WBC) is limited we cannot claim the same evidence for those regions. However, a preliminary examination of the Sentinel-1 A/B Doppler shift estimation from swath data do in fact also reveal promising capabilities for the detection of WBC (personal communication Fabrice Collard). Reprocessing of the full Sentinel-1 A/B data set using the novel calibration for the attitude bias correction is therefore strongly recommended for further improvement of the GMF accuracy and subsequent regular use of the Sentinel-1 A/B for ocean surface current monitoring since the corresponding launches in 2014/2016.

Data Availability Statement

The full collocated data set (including re-calibrated Sentinel-1 observations) is available as the supplementary information for the review propose. It will be openly published in open access PANGEEA repository by acceptance of the paper.

Acknowledgments
This work was performed under NERSC 251348/F50 and CIRFA 970422528 projects funded by the Norwegian Research Council. We would also like to thank ESA-ESRIN Sentinel 1 RVL Assessment Project and the Copernicus program for providing open access to the Sentinel-1B WV L2 OCN products. The Doppler attitude bias corrections based on the Gyroscope data were provided by OceanDataLab, while IFREMER provided access to WAVEWATCHIII simulations. NOAA AOML is thanked for providing open access to the surface drifter climatology.

References

Abadi, M., Agarwal, A., Barham, P., Brevdo, E., Chen, Z., Citro, C., et al. (2015). TensorFlow: Large-scale machine learning on heterogeneous systems. Retrieved from http://download.tensorflow.org/paper/whitepaper2015.pdf

Alpers, W., & Hennings, I. (1984). A theory of the imaging mechanism of underwater bottom topography by real and synthetic aperture radar. *Journal of Geophysical Research*, *89*(C6), 10,529–10,546. https://doi.org/10.1029/JC089iC06p10529

Ardhuin, F., Gille, S. T., Menemenlis, D., Rocha, C. B., Rascle, N., Chapron, B., et al. (2017). Small-scale open ocean currents have large effects on wind wave heights. *Journal of Geophysical Research: Oceans*, *122*, 4500–4517. https://doi.org/10.1002/2016JC012413

Chapron, B., Collard, F., & Ardhuin, F. (2005). Direct measurements of ocean surface velocity from space: Interpretation and validation. *Journal of Geophysical Research*, *110*, C07008. https://doi.org/10.1029/2004JC002809

Chapron, B., Collard, F., & Kerbaol, V. (2004). *Satellite synthetic aperture radar sea surface Doppler measurements* (pp. 133–141). Paper presented at 2nd Workshop on Coastal and Marine Applications of Synthetic Aperture Radar.

Collecte Localisation Satellites. (2019). S-1A & S-1B annual performance report for 2018. ESA.

Collard, F., Mouche, A., Chapron, B., Danilo, C., & Johannessen, J. (2008). *Routine high resolution observation of selected major surface currents from space*. Paper presented at Proceedings of SEASAR 2008, Frascati.

Collecte Localisation Satellites. (2019). Sentinel-1 product specification. S1-RS-MDA-52-7441. ESA.

Copernicus. (2017-2018). Sentinel data. processed by ESA.
Hansen, M. W., Collard, F., Dagestad, K.-F., Johannessen, J., Fabry, P., & Chapron, B. (2011). Retrieval of sea surface range velocities from Envisat ASAR Doppler centroid measurements. *IEEE Transactions on Geoscience and Remote Sensing*, *49*(10 PART 1), 3582–3592. https://doi.org/10.1109/TGRS.2011.2153864
Johannessen, J. A., Chapron, B., Collard, F., Kudryavtsev, V., Mouche, A., Akimov, D., & Dagestad, K. F. (2008). Direct Ocean surface velocity measurements from space: Improved quantitative interpretation of Envisat ASAR observations. *Geophysical Research Letters*, *35*, L22608. https://doi.org/10.1029/2008GL035709
Johnsen, H., Nilsen, V., Engen, G., Mouche, A., & Collard, F. (2016). *Ocean doppler anomaly and ocean surface current from Sentinel-1 TOPS mode* (pp. 3993–3996). Paper presented at 2016 International Geoscience and Remote Sensing Symposium (IGARSS), Beijing. https://doi.org/10.1109/IGARSS.2016.7730038
Kudryavtsev, V., Yurovskaya, M., Chapron, B., Collard, F., & Donlon, C. (2017). Sun glitter imagery of surface waves. Part 2: Waves transformation on ocean currents. *Journal of Geophysical Research: Oceans*, *122*, 1384–1399. https://doi.org/10.1002/2016JC012426
Laurindo, L. C., Marian, A. J., & Lumpkin, R. (2017). An improved near-surface velocity climatology for the global ocean from drifter observations. *Deep Sea Research Part I: Oceanographic Research Papers*, *124*, 73–92. https://doi.org/10.1016/j.dsr.2017.04.009
Martin, A., Gommenginger, C., Marquez, J., Doody, S., Navarro-Sanchez, V., & Buck, C. (2016). Wind-wave induced velocity in ATI SAR ocean surface currents: First experimental evidence from an airborne campaign. *Journal of Geophysical Research: Oceans*, *121*, 1640–1653. https://doi.org/10.1002/2015JC011459
Moiseev, A., Johnsen, H., Hansen, M. W., & Johannessen, J. A. (2020). Evaluation of radial ocean surface currents derived from Sentinel-1 IW Doppler shift using coastal radar and Lagrangian surface drifter observations. *Journal of Geophysical Research: Oceans*, *125*, e2019JC015743. https://doi.org/10.1029/2019JC015743
Mouche, A., & Chapron, B. (2015). Global C-band Envisat, RADARSAT-2 and Sentinel-1 SAR measurements in copolarization and cross-polarization. *Journal of Geophysical Research: Oceans*, *120*, 7195–7207. https://doi.org/10.1002/2015JC011149
Mouche, A., Chapron, B., Reul, N., & Collard, F. (2008). Predicted Doppler shifts induced by ocean surface wave displacements using asymptotic electromagnetic wave scattering theories. *Waves in Random and Complex Media*, *18*(1), 185–196. https://doi.org/10.1080/17455030701564644
Mouche, A. A., Collard, F., Chapron, B., Dagestad, K. F., Guitton, G., Johannessen, J. A., & Hansen, M. W. (2012). On the use of doppler shift for sea surface wind retrieval from SAR. *IEEE Transactions on Geoscience and Remote Sensing*, *50*(7 PART 2), 2901–2909. https://doi.org/10.1109/TGRS.2011.2174998
Nouguier, F., Chapron, B., Collard, F., Mouche, A., Rascle, N., Ardhuin, F., & Wu, X. (2018). Sea surface kinematics from near-nadir radar measurements. *IEEE Transactions on Geoscience and Remote Sensing*, *56*(10), 6169–6179. https://doi.org/10.1109/TGRS.2018.2833200
OceanDataLab. (2019). S-1 RVL DIL4: Algorithm description document. ESRIN: ESA.
Romeiser, R., & Thompson, D. (2000). Numerical study on the along-track interferometric radar imaging mechanism of oceanic surface currents. *IEEE Transactions on Geoscience and Remote Sensing*, *38*(1), 446–458. https://doi.org/10.1109/36.823940
Stopa, J., Ardhuin, F., Chapron, B., & Collard, F. (2015). Estimating wave orbital velocity through the azimuth cutoff from space-borne satellites. *Journal of Geophysical Research: Oceans*, *120*, 7616–7634. https://doi.org/10.1002/2015JC011275
Tolman, H. L. (2009). *User manual and system documentation of WAVEWATCH III TM version 3.14 (Technical note, MMAB Contribution)* (Vol. 276, p. 220).
Yurovsky, Y., Kudryavtsev, V., Grodsky, S., & Chapron, B. (2019). Sea surface Ka-band Doppler measurements: Analysis and model development. *Remote Sensing*, *11*, 839. https://doi.org/10.3390/rs11070839

Graphic design: Communication Division, UiB / Print: Skipnes Kommunikasjon AS

uib.no

ISBN: 9788230861400 (print)
9788230841563 (PDF)